Supporting Information for

Single-atom Co dispersed on polyoxometalate derivatives confined in bamboo-like carbon nanotubes enabling efficient dual-site lattice oxygen mediated oxygen evolution electrocatalysis for acidic water electrolyzers

Jianyun Liu, [a] Tanyuan Wang, *[a] Zijie Lin, [a] Mengyi Liao, [a] Shuxia Liu, [a] Shiyu Wang, [a] Zhao Cai, [b] Hao Sun, [c] Yue Shen, [a] Yunhui Huang, [a] Qing Li, *[a]

a. State Key Laboratory of Material Processing and Die & Mould Technology School of Materials Science and Engineering, Huazhong University of Science and Technology, Wuhan, 430074, China.

E-mail: wangty@hust.edu.cn, qing_li@hust.edu.cn

b. Faculty of Materials Science and Chemistry, China University of Geosciences (Wuhan), Wuhan 430074, China

c. Frontiers Science Center for Transformative Molecules, School of Chemistry and Chemical Engineering, and Zhangjiang Institute for Advanced Study, Shanghai Jiao Tong University, Shanghai 200240, China.

Supplemental Experimental Procedures

Fabrication of cyclic macromolecular Mo-Ce polyoxometalates precursors and amorphous Mo-Ce oxides: The cyclic macromolecular Mo-Ce polyoxometalates was synthesized in accordance with published procedures [1]. Specifically, $CeCl_3 \cdot 7H_2O$ (20 mg, 0.05 mmol, Innochem, China) and hydrazine dihydrochloride (3 mg, 0.02 mmol, Innochem, China) were dissolved in 5 mL of deionized water. Then, 1 M HCl (0.4 mL, 0.4 mmol) were added with stirring. Subsequently, $Na_2MoO_4 \cdot 2H_2O$ (50 mg, 0.2 mmol, Aladdin, China) were added to the mixture. When the pH value of the solution reached around 1.8, the mixture was placed in an oven at 100 °C for 3-4 days to form dark blue rhombic shaped crystals. After the reaction, the samples were centrifuged and separated with a mixture of ethanol and deionized water several times. This material was named as Mo-Ce POMs. Afterwards, the synthesized precursor was annealed in N_2 at 400 °C for 2 h, which named as $MoCeO_x$.

Fabrication of amorphous Mo-Ce oxides supported single-atom Co catalysts: To synthesize amorphous Mo-Ce oxides supported single-atom Co oxides, we added $CoCl_2 \cdot 6H_2O$ as the cobalt source during the synthesis of Mo-Ce polyoxometalates precursors. In particular, we dissolved $CeCl_3 \cdot 7H_2O$ (20 mg, 0.05 mmol, Innochem, China), hydrazine dihydrochloride (3 mg, 0.02 mmol, Innochem, China) and $CoCl_2 \cdot 6H_2O$ (11.9 mg, 0.05 mmol, Aladdin, China) in 5 mL of deionized water. Other synthesis methods are the same as cyclic macromolecular Mo-Ce polyoxometalates precursors catalysts. And this sample is named as Co_{SA}-Mo-Ce POMs. To study the effect of Co content on the OER activity, 0. 005, 0.05 and 0.15 mmol $CoCl_2 \cdot 6H_2O$ were

added in 5 mL of deionized water, and the resulting precursors were named as $Co_{SA0.1}$-Mo-Ce POMs, Co_{SA}-Mo-Ce POMs, Co_{SA3}-Mo-Ce POMs, which based on the proportion of the precursor input. Then, the synthesized precursors were annealed in N_2 at 400 °C for 2 h, and these samples were named as $Co_{SA0.09}$-$MoCeO_x$, Co_{SA}-$MoCeO_x$, and $Co_{SA1.81}$-$MoCeO_x$, respectively.

Fabrication of bamboo-like carbon nanotubes (BCT): First, dicyandiamide (5.0 g, Innochem, China) and $CoCl_2 \cdot 6H_2O$ (2.2 g, Aladdin, China) were dissolved in 300 ml of deionized water and stirred for dry at 100 °C. Afterwards, the mixture was taken out and ground into powder, and then the powders were annealed in Ar at 800 °C for 1 h. Subsequently, the heat-treated samples were leached in 2 M HCl for 24 h to remove the metal particles remaining in catalysts. Finally, this sample was centrifuged and separated with a mixture of ethanol and deionized water several times and dried at 80 °C.

Fabrication of amorphous Mo-Ce oxides supported single-atom Co catalysts coated with bamboo-like carbon nanotubes (Co_{SA}-$MoCeO_x$@BCT): BCT (25 mg) was put into a three-necked flask with an air valve, and evacuated to ca. 30 Pa. Then, the ethanol mixture (20 ml) dissolved with 25 mg Co_{SA}-Mo-Ce POMs precursor was quickly dropped into the three-necked flask and magnetically stirred for 5 h. The sample was filtrated and freeze-dried, then washed repeatedly with deionized water and dried under vacuum. Then, the as-prepared ground samples were put into a tube furnace and heated at 400 °C for 2 hours in a N_2 gas flow. This sample was named as Co_{SA}-$MoCeO_x$@BCT.

Fabrication of Co_{SA}-$MoCeO_x$@BCT loaded electrodes: The electrocatalysts (5 mg) and

Vulcan XC-72 carbon powder (5 mg) were dispersed in a mixture of 1 ml of deionized water and isopropanol (Aladdin, China) with a volume ratio of 3: 1, with 40 µl of 5% Nafion solution as a binder. After ultrasonication for 30 minutes, 30 µl of homogeneous ink was dropped on a carbon paper substrate (Fuel Cell Earth, TGP-H-060) (area, 0.25 cm^2) and fully dried in air at room temperature. The mass loadings of the electrocatalysts onto carbon paper were controlled at approximately 0.6 mg cm^{-2}.

Fabrication of IrO_2/C and Pt/C loaded electrodes: IrO_2/C commercial catalysts (Aladdin, China, 99%) or 20% Pt/C commercial catalysts (Johnson Matthey, USA, 99%) were dispersed in 1 ml of isopropanol with 40 µl of 5% Nafion and ultrasonicated for 30 minutes. Later, the solution was loaded on the surface of a carbon paper substrate (Fuel Cell Earth, TGP-H-060) (area, 0.25 cm^2) with a loading of 0.6 mg cm^{-2} for IrO_2 or 20% Pt/C catalysts.

Material characterizations: Infrared spectroscopy were collected in transmission mode using an ATR fitted Nicolet iS50R spectrometer (Thermo Scientific, USA). UV-vis spectra were recorded on a Lambda 35 spectrophotometer (PerkinElmer, USA) using 1 cm pathlength cuvettes. Thermogravimetric analysis characterizations were performed on a Pyris1 TGA Thermogravimetric analyzers (PerkinElmer Instruments, China) under N_2 atmosphere with a heating rate of 10 ^oC min^{-1}. Mass spectrometry characterization were performed on a bruker ultraflextreme MALDI-TOF/TOF instrument (Bruker, USA). Transmission electron microscopy (TEM) characterizations were obtained on a Tecnai G2 transmission electron microscope (FEI, USA). High-resolution transmission electron microscope (HR-TEM) was carried out by a Talos

F200X transmission electron microscope (FEI, Netherlands). X-ray diffraction (XRD) patterns were obtained using a DMAX-2400X-ray diffractometer (Rigaku, Japan). Raman measurements were performed using a LabRAM HR Evolution (Horiba JobinYvon, France) with 532 nm excitation wavelength. X-ray photoelectron spectroscopy (XPS) was carried out with an Axis-Ultra DLD-600W X-ray photoelectron spectrometer (Shimazu, Japan). X-ray fluorescence (XRF) patterns were obtained from EAGLE III operated at 40 kV. Inductively coupled plasma-optical emission spectrometry (ICP-OES) were carried out by an iCE 3000 Series AA spectrometer (Thermo Scientific, USA). X-ray absorption spectroscopy (XAS) was determined by the XAS measurement at the beamline BL11B1 of the shanghai Synchrotron Radiation Facility (SSRF).

Electrochemical characterization: The OER polarization curves were carried out with a CHI 760D (Chenhua, China) electrochemical workstation in 0.5 M H_2SO_4 electrolyte in a typical three-electrode system with a scan rate of 5 mV s^{-1} at room temperature. The as-prepared Co_{SA}-$MoCeO_x$@BCT sample was used as the working electrode for electrochemical characterizations, the Ag/AgCl reference electrode was used as reference electrode and a commercial carbon rod was used as counter electrode. The potential was calibrated to reversible hydrogen electrode (RHE) through measuring the potential difference between the Ag/AgCl reference electrode and RHE. The Faraday efficiency of $MoCeO_x$, Co_{SA}-$MoCeO_x$ and Co_{SA}-$MoCeO_x$@BCT samples were carried on a Shimadzu GC-2014 gas chromatograph (Shimadzu, Japan) in 0.5 M H_2SO_4 electrolyte to analyze the composition of gas products by using a two-electrode system

(Pt/C catalysts as the cathode). The long-time overall acid solution water splitting stability curves were carried on a LAND C3001B battery measurement system (Wuhan, China) in 0.5 M H_2SO_4 electrolyte and the Co_{SA}-$MoCeO_x$@BCT electrodes and commercial Pt/C materials were used as anode and cathode, respectively. All electrochemical measurements do not have any iR compensation.

Electrochemical impedance spectroscopy measurements: To evaluate the charge transfer resistance, electrochemical impedance spectroscopy measurements were carried out by applying an AC voltage of 10 mV in the frequency range of 100000-0.1 Hz at 1.47 V (vs RHE).

Proton exchange membrane water electrolyzers (PEMWEs): Membrane electrode assemblies (MEAs) were prepared using a Nafion®117 polymer membrane (DuPont, thickness 177.8 μm, N117). Before MEAs preparation, the N117 membrane was boiled separately for half an hour in the following solutions to remove possible contaminants and ensure complete protonation: first 3 wt.% H_2O_2, then Milliq ultra-pure water, then 1.0 M H_2SO_4, and finally Milliq ultra-pure water. Finally, the N117 film is dried in a 40 °C oven for several hours before use. Co_{SA}-$MoCeO_x$@BCT materials and the commercial Pt/C catalysts were used as the anode and cathode, and the mass loadings were controlled at 3.2 mg cm^{-2} of Co_{SA}-$MoCeO_x$@BCT and 0.2 mg cm^{-2} of commercial Pt/C catalysts, respectively. The effective area of the MEA was 5 cm^2. Electrolysis tests were conducted using a single cell PEMWE. The titanium meshes were used as gas diffusion layers for both the anode and cathode. During the test, the cell was maintained at room temperature, and the pre-heated DI water was fed to the

anode at a flow rate of 10 ml min^{-1} (pipe diameter 4.8 mm).

In situ Raman experimental details: Raman measurements were performed using a LabRAM HR Evolution (Horiba JobinYvon, France) with 532 nm excitation wavelength. Before the test, the samples and Vulcan XC-72 carbon powder were dropped on a carbon paper substrate (Fuel Cell Earth, TGP-H-060) (area, 1 cm^2) at a ratio of 1:1 and fully dried in air at room temperature. The mass loading of the electrocatalysts on the carbon paper were controlled at about 0.6 mg cm^{-2}. All the *in situ* spectra were collected in an *in situ* Raman gas diffusion H-type electrolytic cell (gaossunoin, China) with 0.5 M H_2SO_4 as the electrolyte after the samples were operated at constant voltage for 5 min.

Operando x-ray absorption structure (XAS) spectroscopy experimental details: The *operando* Co K-edge XAS spectroscopy of the Co_{SA}-$MoCeO_x$ electrocatalyst were collected on the beamline BL11B1 of the shanghai Synchrotron Radiation Facility (SSRF). A cobalt foil is used to calibrate the energy. During the *operando* XAS measurements, the method of constant potential is applied. *Operando* XAS spectroscopy signals were collected in fluorescence mode using an in situ electrochemical cell with polyimide film windows (XAFS-2, gaossunoin, China). To monitor the changes of electrodes during the OER process, anodic voltages from 1.1 to 1.5 V versus RHE are applied for Co_{SA}-$MoCeO_x$ catalysts, respectively. For each XAS spectroscopy collection, the selected constant potential is first applied to the electrodes in 0.5 M H_2SO_4 electrolyte for 10 min as the pretreatment step. Subsequently, the XAS spectra of electrocatalysts are collected through a fluorescence mode within 30 min. It

would take about 40 min for the XAS measurement under each constant potential applied. The data reductions of the experimental spectra to normalized XANES and Fourier-transformed radial distribution functions (RDFs) were performed through the standard XAS procedure.

Lattice oxygen ion diffusion coefficients measurement: The same three-electrode configuration was used for the measurement, and the LSV scanning was performed in sulfuric acid solutions with pH=0, 1, 2, and 3 respectively to obtain the OER polarization curves with a scan rate of 5 mV s^{-1} at room temperature. The electrolytic current density of water splitting was recorded under the voltage of 1.6 V, and linear fitting was performed to estimate the oxygen ion diffusion coefficient of different samples.

In situ ^{18}O isotope labeling differential electrochemical mass spectrometry (DEMS) experimental details: The *in situ* DEMS experiments of the Co_{SA}-$MoCeO_x$@BCT electrocatalyst on an *in situ* differential electrochemical mass spectrometer provided by Linglu Instruments (QAS100, Shanghai) Co. Ltd. First, pristine samples were isotopically labeled with ^{18}O in ^{18}O-labeled 0.5 M H_2SO_4 solution at 1.5 V for 10 min. The resultant electrodes were then rinsed several times with $H_2{}^{16}O$ and dried in an oven to remove residual $H_2{}^{18}O$. After these processes, the samples were subjected to chronoamperometry at 1.5 V for *in situ* DEMS measurements. To exclude the influence of ^{18}O natural abundance, the mass signal of $^{34}O_2$ is normalized by the total signal intensity of $^{36}O_2$ obtained in the same test, and the total signal intensity of $^{32}O_2$ and $^{34}O_2$ is defined as the integrated area of the intensity curve.

Computational methods: Spin-polarized DFT calculations were performed using the Vienna ab initio simulation package (VASP). [2] [3] The generalized gradient approximation proposed by Perdew, Burke, and Ernzerhof (GGA-PBE) is selected for the exchange-correlation potential. [4] The pseudo-potential was described by the projector-augmented-wave (PAW) method. [5] The geometry optimization is performed until the Hellmann–Feynman force on each atom is smaller than 0.02 $eV \cdot Å^{-1}$. The energy criterion is set to 10^{-6} eV in iterative solution of the Kohn-Sham equation.

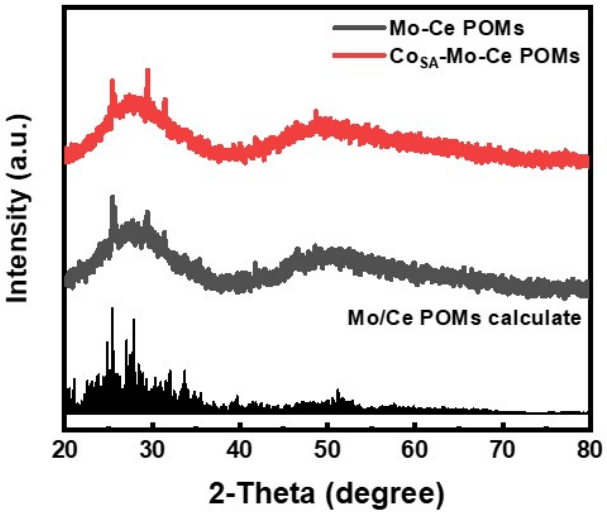

Fig. S1 XRD patterns of Mo-Ce POMs and Co_{SA}-Mo-Ce POMs, respectively.

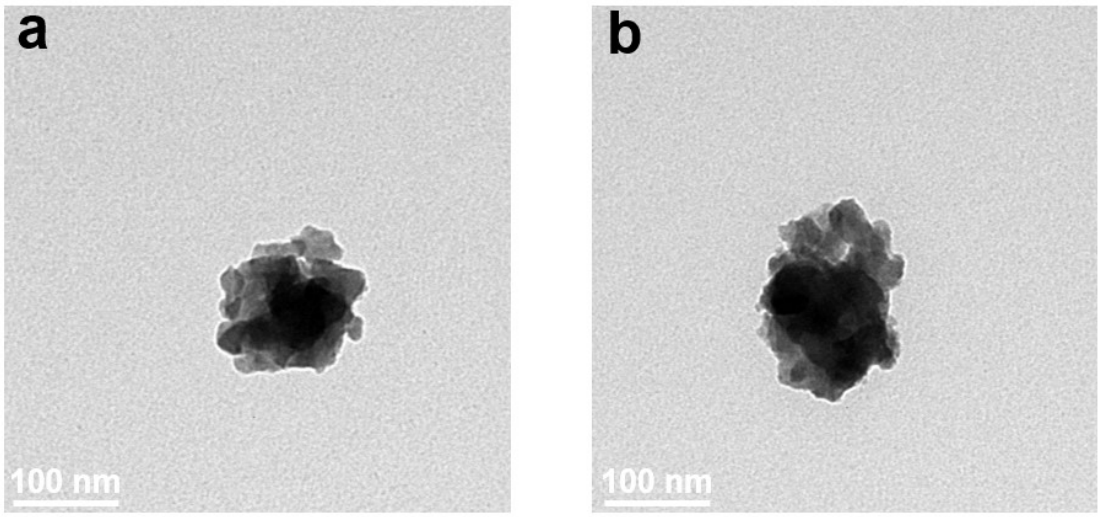

Fig. S2 TEM images of Mo-Ce POMs and Co_{SA}-Mo-Ce POMs, respectively.

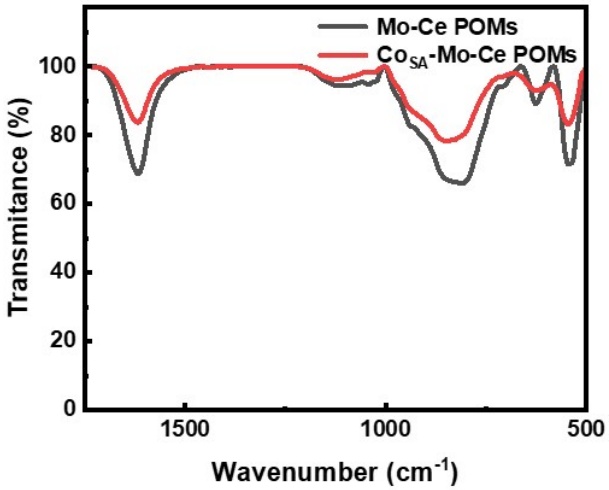

Fig. S3 IR spectrum of Mo-Ce POMs and Co_{SA}-Mo-Ce POMs, respectively.

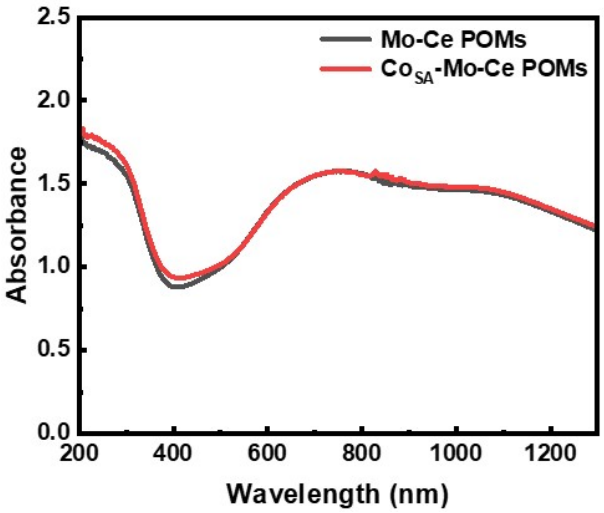

Fig. S4 UV-VIS spectrums of Mo-Ce POMs and Co_{SA}-Mo-Ce POMs, respectively.

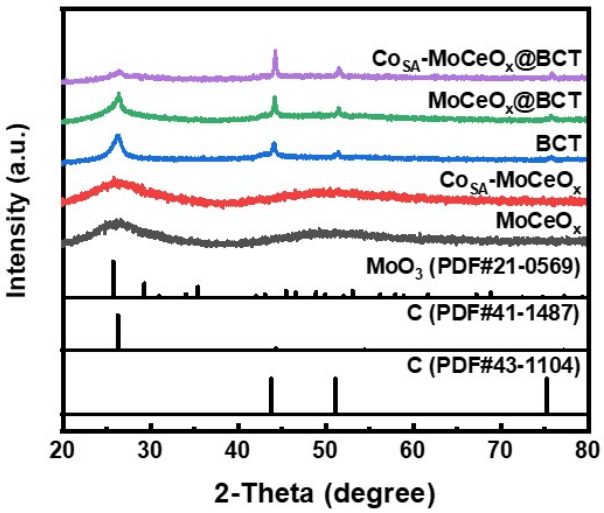

Fig. S5 XRD patterns of $MoCeO_x$, Co_{SA}-$MoCeO_x$, BCT, $MoCeO_x$@BCT and Co_{SA}-$MoCeO_x$@BCT.

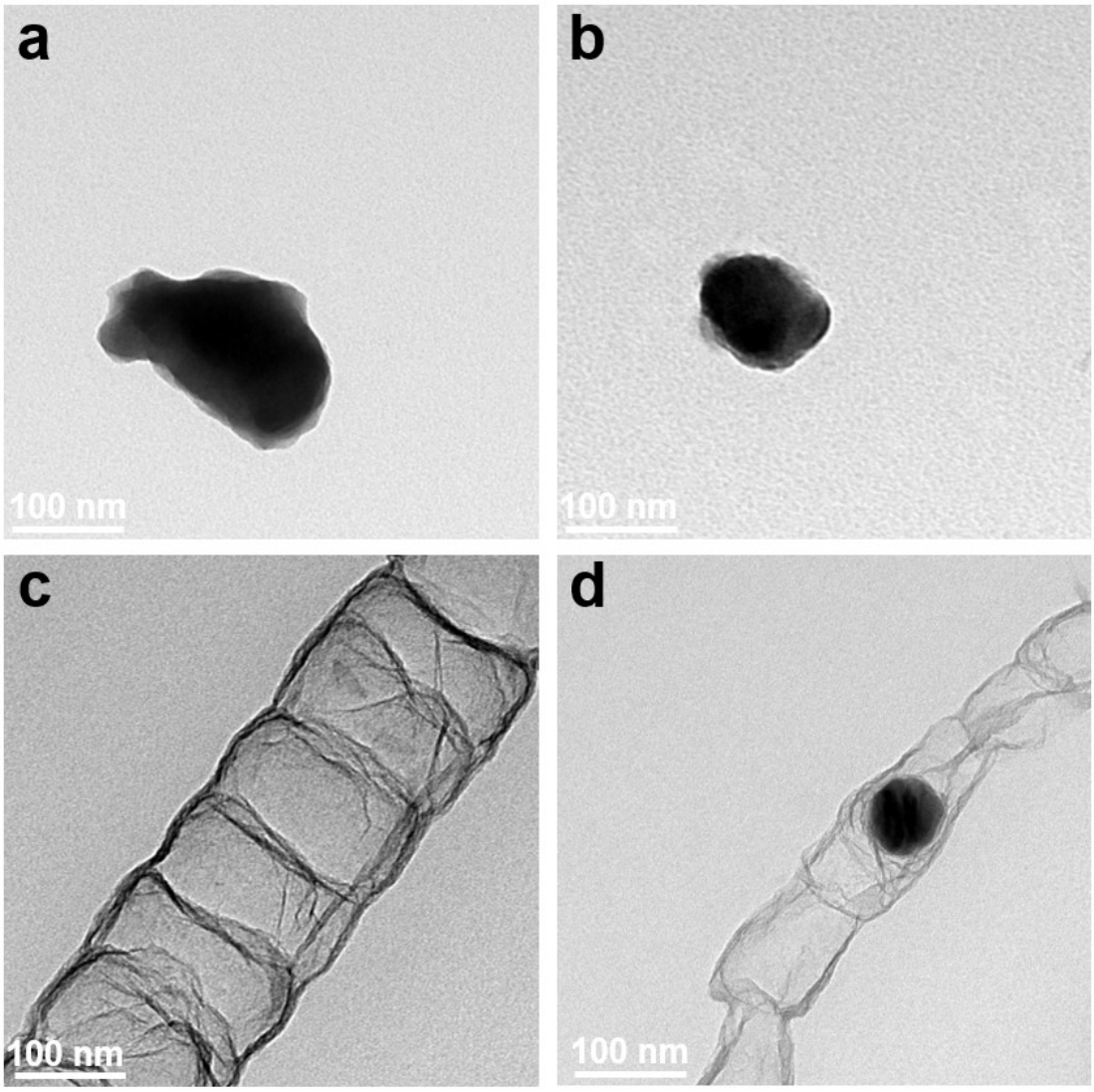

Fig. S6 TEM images of (a) $MoCeO_x$, (b) Co_{SA}-$MoCeO_x$, (c) BCT and (d) $MoCeO_x$@BCT, respectively.

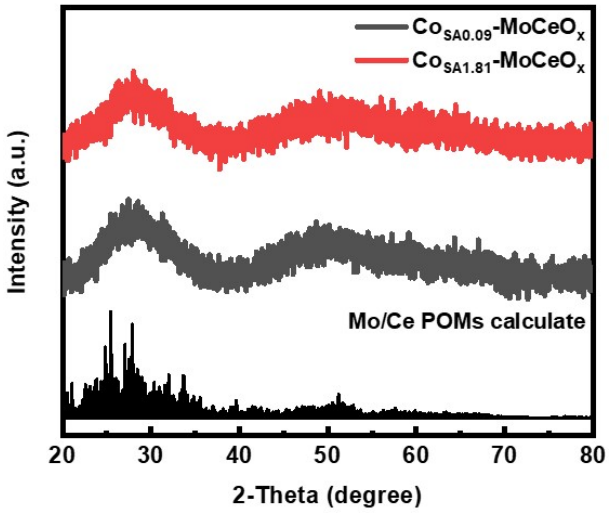

Fig. S7 XRD patterns of $Co_{SA0.09}$-$MoCeO_x$ and $Co_{SA1.81}$-$MoCeO_x$, respectively.

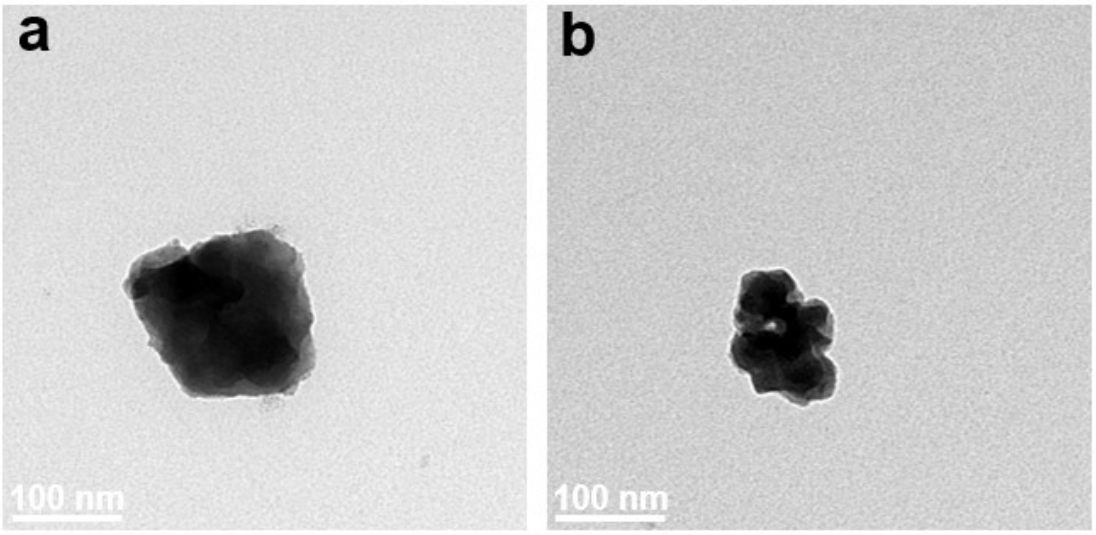

Fig. S8 TEM images of $Co_{SA0.09}$-$MoCeO_x$ and $Co_{SA1.81}$-$MoCeO_x$, respectively.

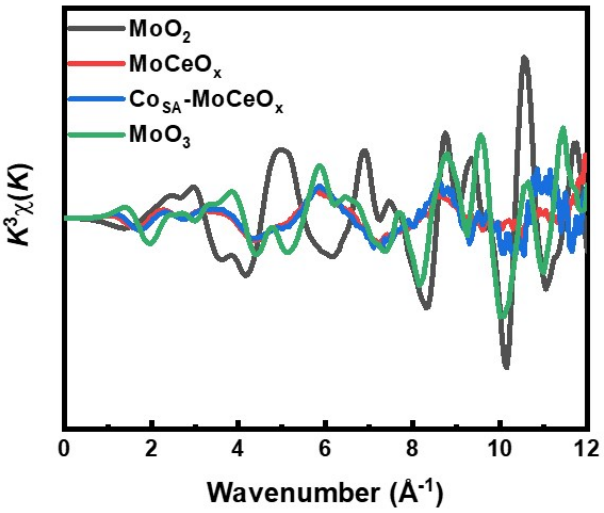

Fig. S9 Fourier transforms of k^3-weighted Mo K-edge EXAFS spectra for k space of MoO_2, $MoCeO_x$, Co_{SA}-$MoCeO_x$ and MoO_3, respectively.

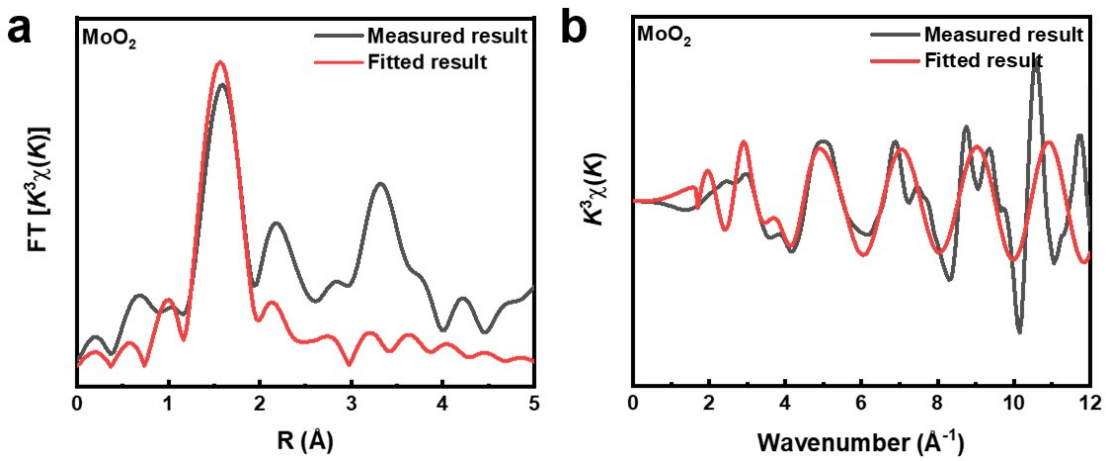

Fig. S10 k^3-weighted EXAFS. (a) r space, (b) k space fitting curves of MoO_2.

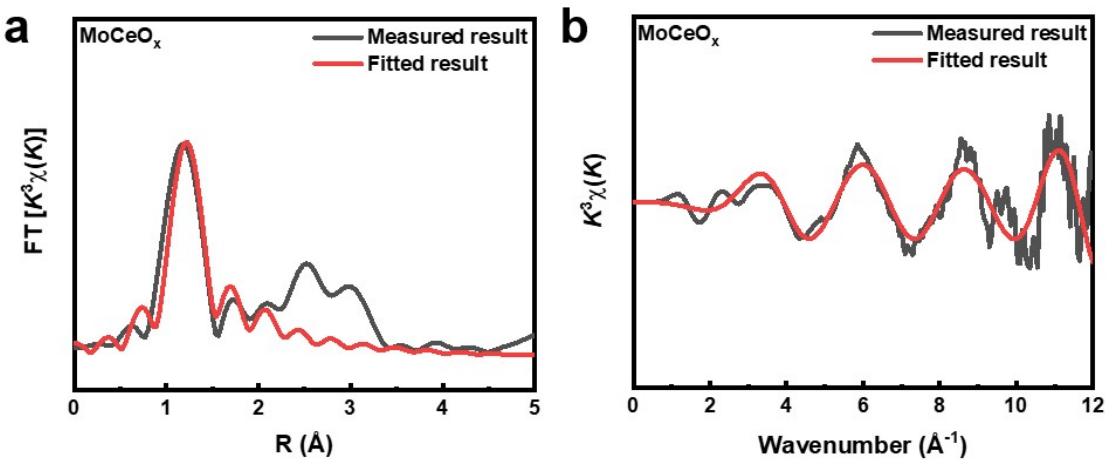

Fig. S11 k^3-weighted EXAFS. (a) r space, (b) k space fitting curves of MoCeO$_x$.

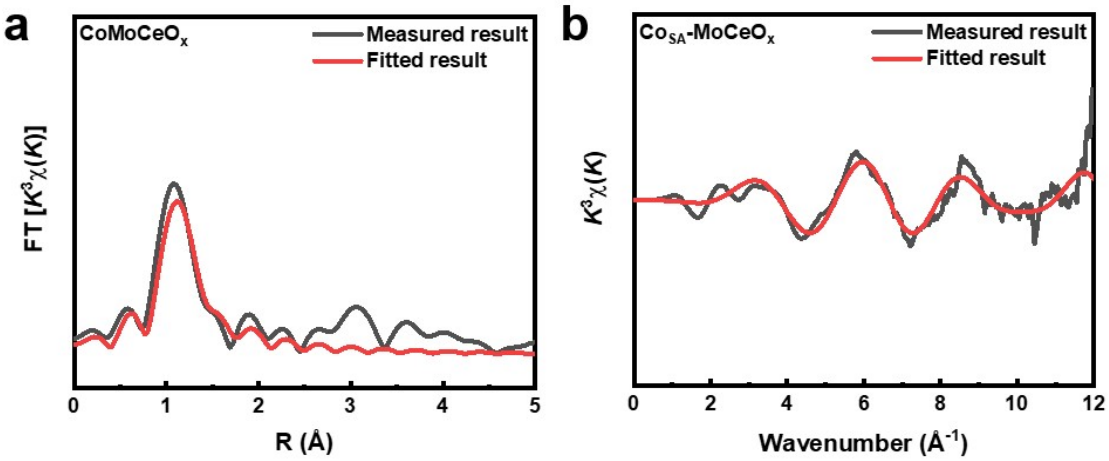

Fig. S12 k^3-weighted EXAFS. (a) r space, (b) k space fitting curves of Co_{SA}-$MoCeO_x$.

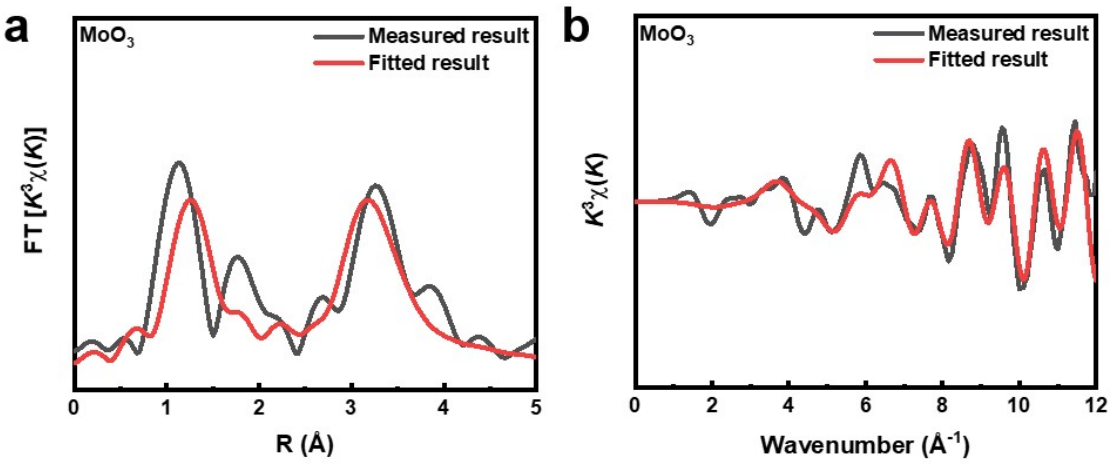

Fig. S13 k^3-weighted EXAFS. (a) r space, (b) k space fitting curves of MoO_3.

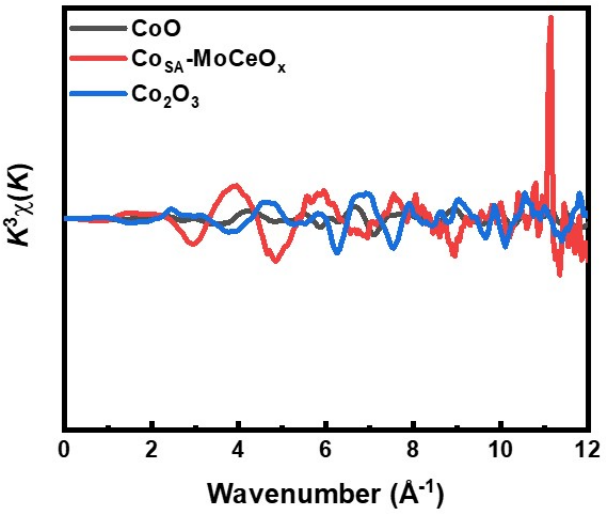

Fig. S14 Fourier transforms of k^3-weighted Co K-edge EXAFS spectra for k space of CoO, $CoMoCeO_x$ and Co_2O_3.

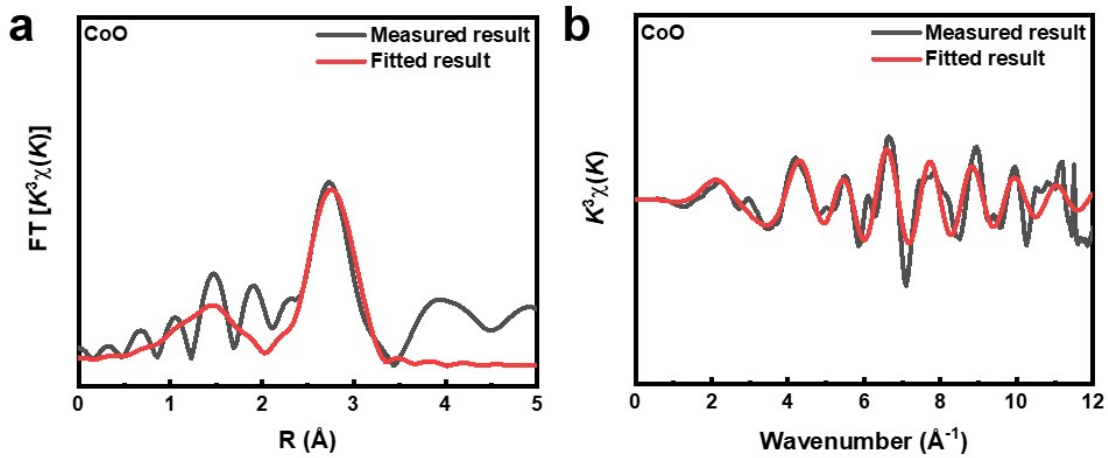

Fig. S15 k^3-weighted EXAFS. (a) r space, (b) k space fitting curves of CoO.

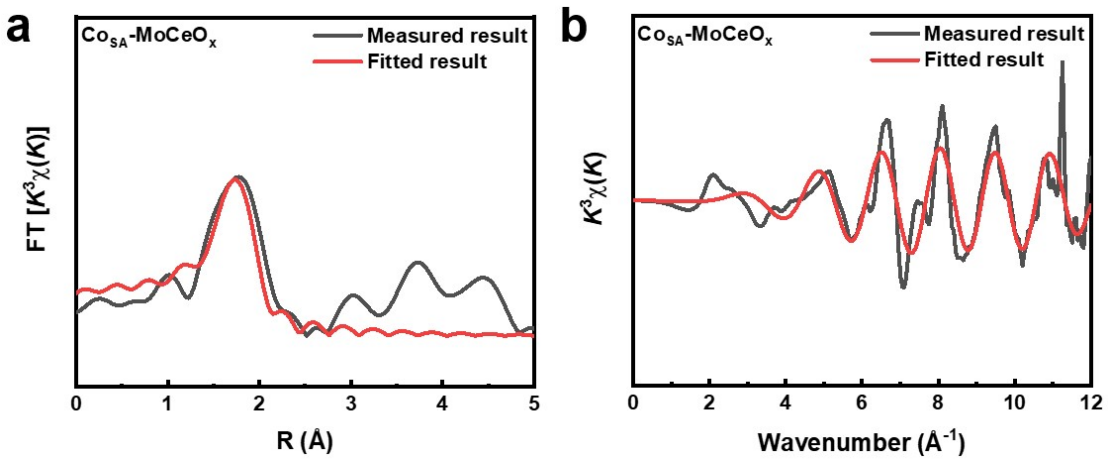

Fig. S16 k^3-weighted EXAFS. (a) r space, (b) k space fitting curves of Co_{SA}-$MoCeO_x$.

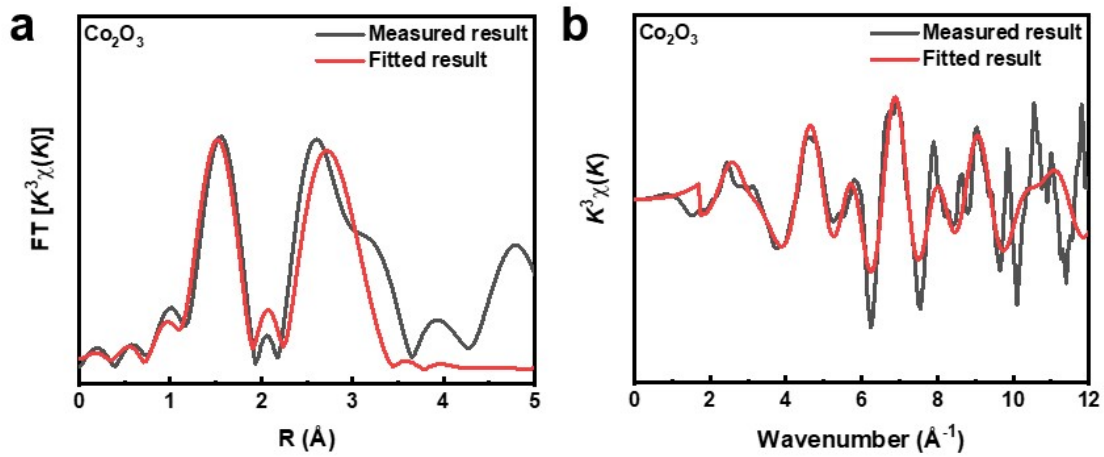

Fig. S17 k^3-weighted EXAFS. (a) r space, (b) k space fitting curves of Co_2O_3.

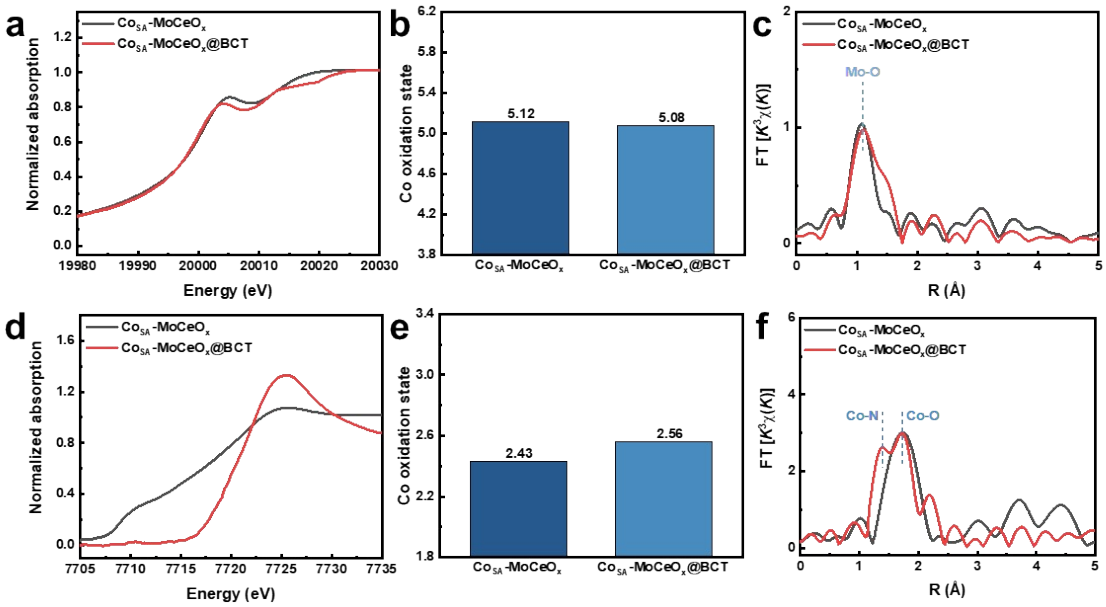

Fig. S18 (a) Mo K-edge XANES spectra of Co_{SA}-$MoCeO_x$ and Co_{SA}-$MoCeO_x$@BCT. (b) The average oxidation state of Mo atoms of Co_{SA}-$MoCeO_x$ and Co_{SA}-$MoCeO_x$@BCT. (c) Fourier transforms of k^3-weighted Mo K-edge EXAFS spectra for r space of Co_{SA}-$MoCeO_x$ and Co_{SA}-$MoCeO_x$@BCT. (d) Co K-edge XANES spectra of Co_{SA}-$MoCeO_x$ and Co_{SA}-$MoCeO_x$@BCT. (e) The average oxidation state of Co atoms of Co_{SA}-$MoCeO_x$ and Co_{SA}-$MoCeO_x$@BCT. (f) Fourier transforms of k^3-weighted Co K-edge EXAFS spectra for r space of Co_{SA}-$MoCeO_x$ and Co_{SA}-$MoCeO_x$@BCT.

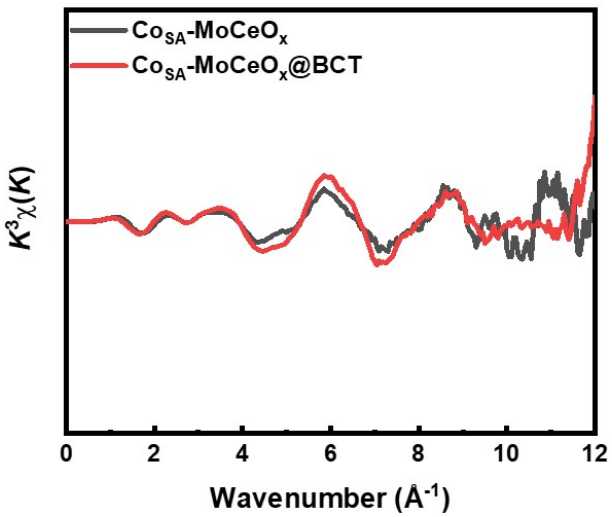

Fig. S19 Fourier transforms of k^3-weighted Mo K-edge EXAFS spectra for k space of Co_{SA}-$MoCeO_x$ and Co_{SA}-$MoCeO_x$@BCT, respectively.

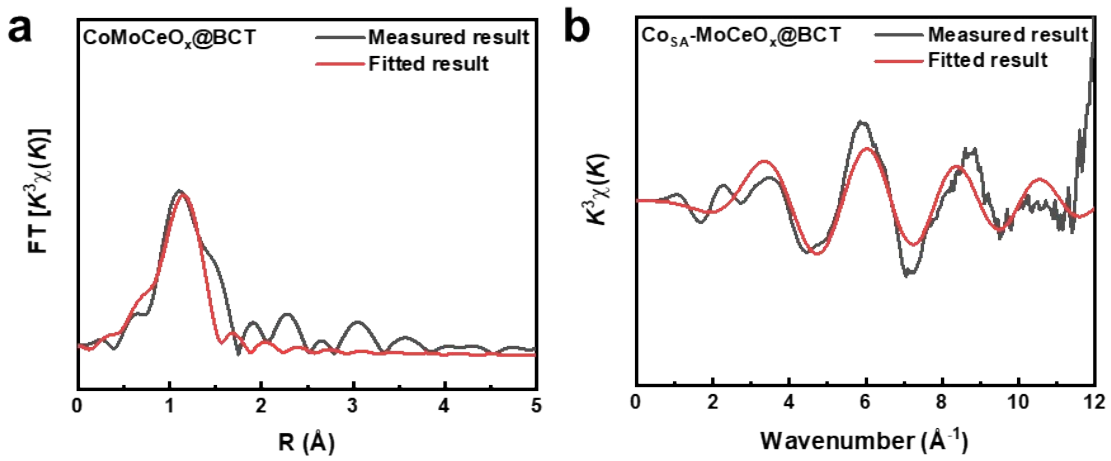

Fig. S20 k^3-weighted EXAFS. (a) r space, (b) k space fitting curves of Co$_{SA}$-MoCeO$_x$@BCT.

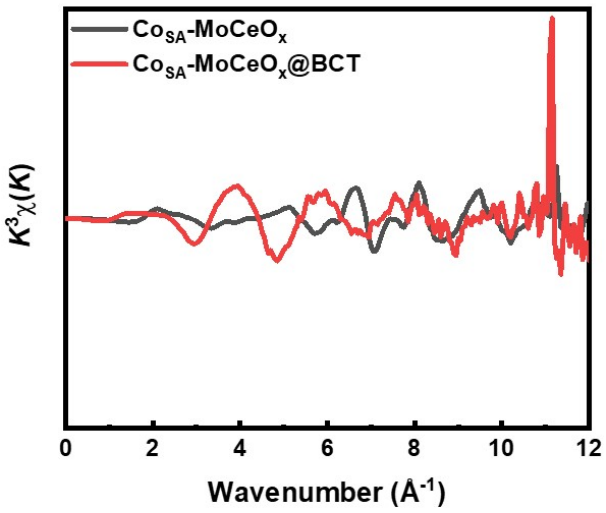

Fig. S21 Fourier transforms of k^3-weighted Co K-edge EXAFS spectra for k space of Co_{SA}-$MoCeO_x$ and Co_{SA}-$MoCeO_x$@BCT, respectively.

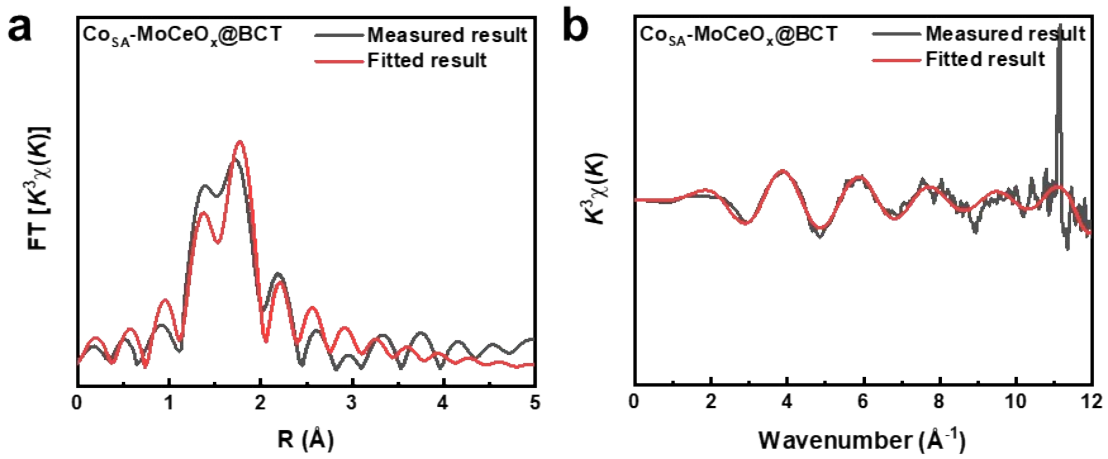

Fig. S22 k^3-weighted EXAFS. (a) r space, (b) k space fitting curves of Co$_{SA}$-MoCeO$_x$@BCT.

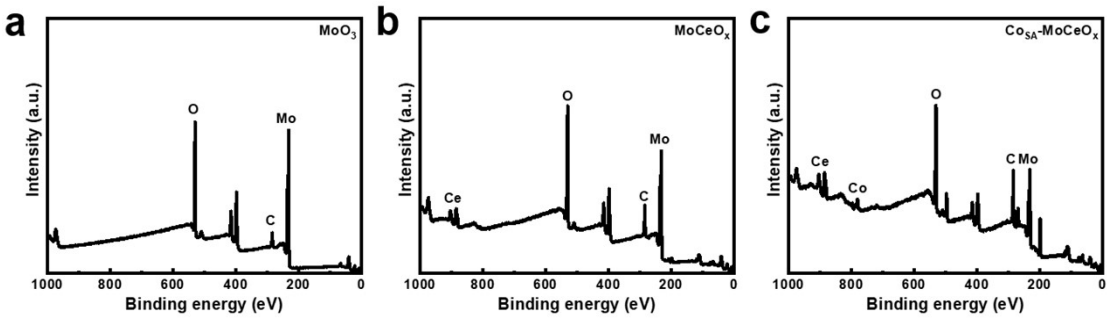

Fig. S23 XPS survey spectra for (a) MoO_3, (b) $MoCeO_x$, (c) Co_{SA}-$MoCeO_x$.

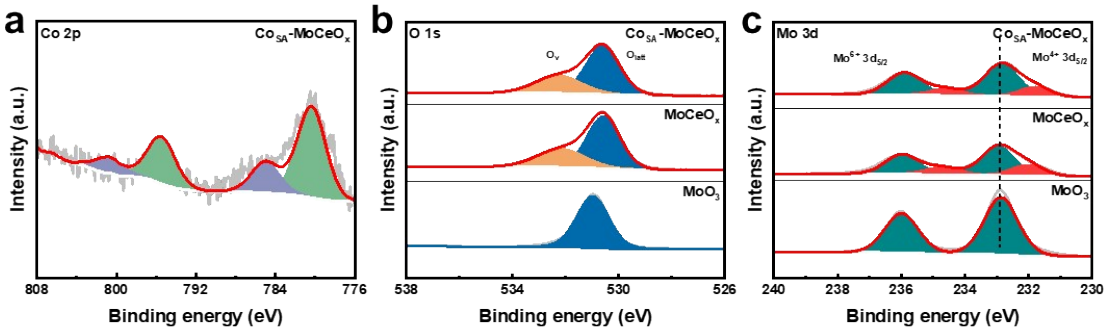

Fig. S24 XPS characterization of MoO_3, $MoCeO_x$ and Co_{SA}-$MoCeO_x$ samples. (a) Mo 3d XPS spectra for MoO_3, $MoCeO_x$ and Co_{SA}-$MoCeO_x$. (b) O 1s XPS spectra for MoO_3, $MoCeO_x$ and Co_{SA}-$MoCeO_x$. (d) Co 2p XPS spectra for Co_{SA}-$MoCeO_x$.

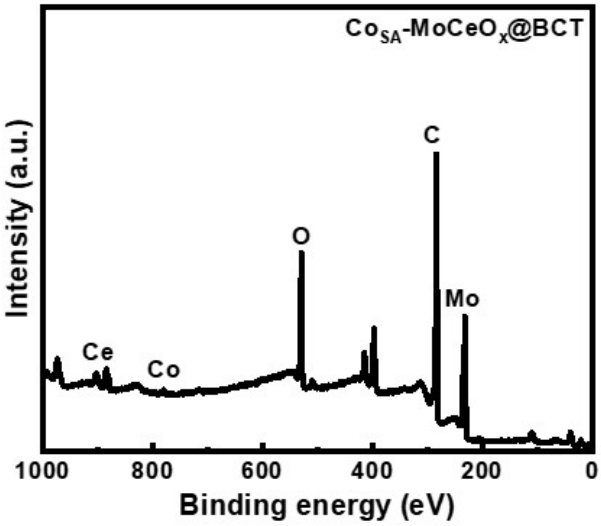

Fig. S25 XPS survey spectra for Co_{SA}-$MoCeO_x$@BCT.

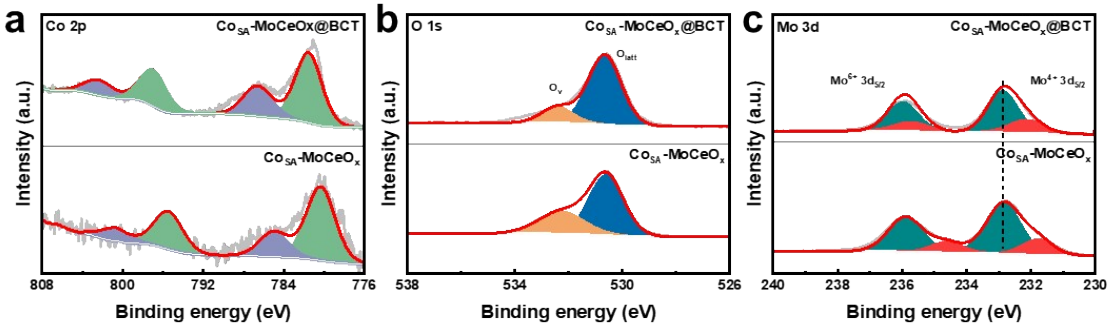

Fig. S26 XPS characterization of (a) Co 3d, (b) O 1s, (c) Mo 2p XPS spectra for Co_{SA}-$MoCeO_x$ and Co_{SA}-$MoCeO_x$@BCT.

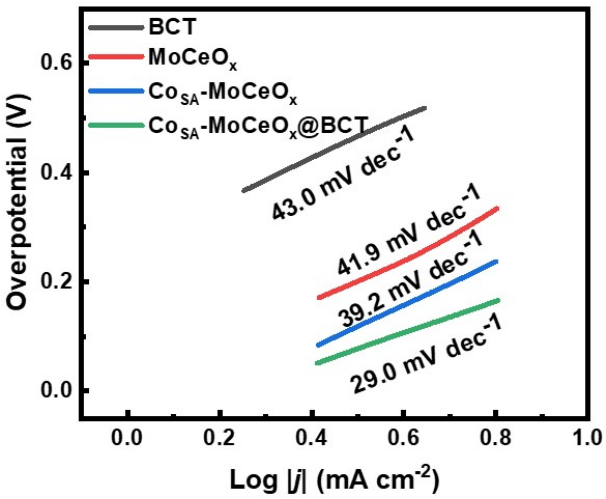

Fig. S27 Tafel plots of BCT, $MoCeO_x$, Co_{SA}-$MoCeO_x$ and Co_{SA}-$MoCeO_x$@BCT.

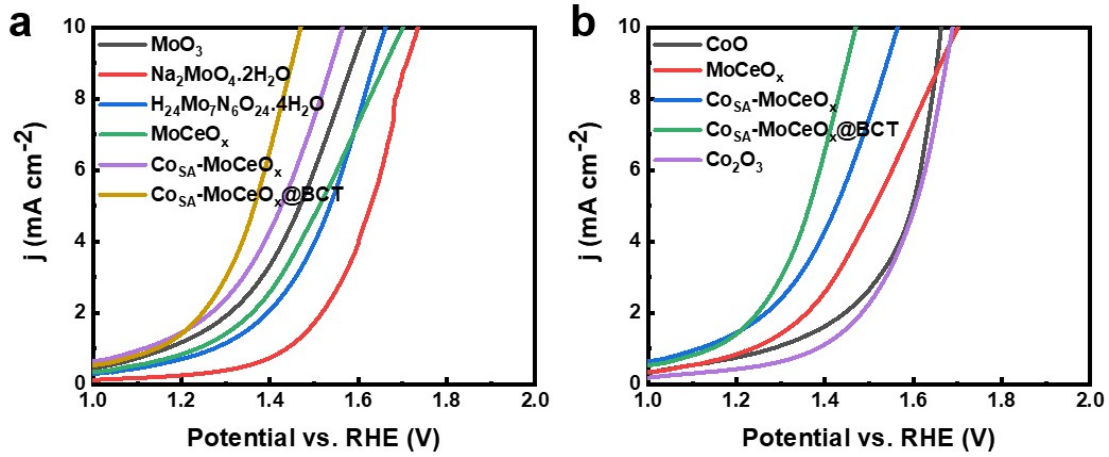

Fig. S28 OER activity of (a) Mo-based catalysts and (b) Co-based oxides in 0.5 M H_2SO_4.

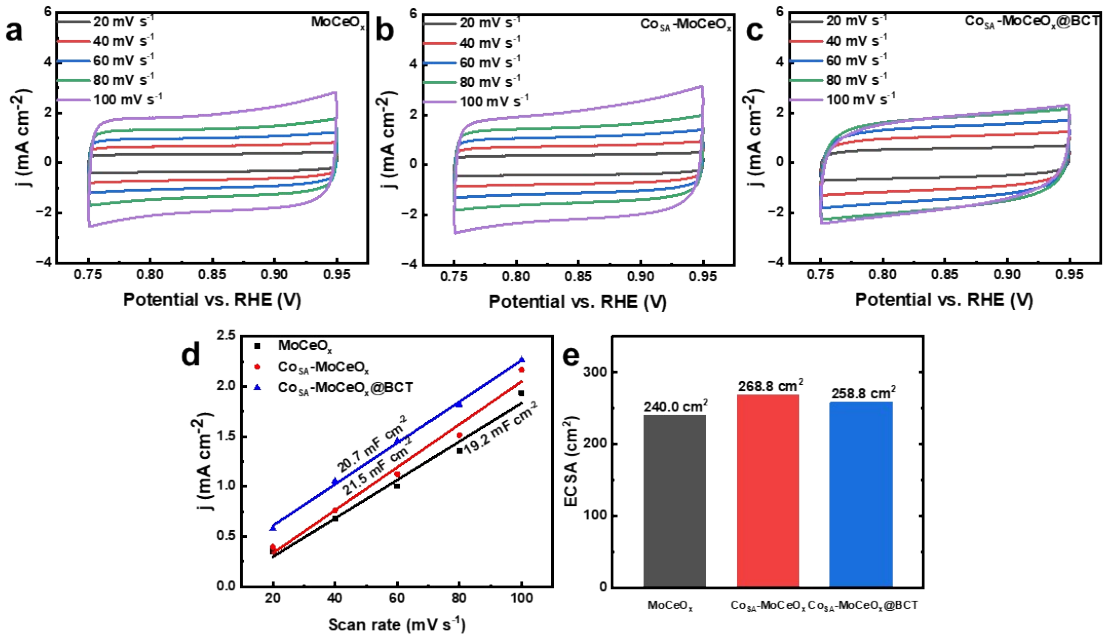

Fig. S29 Electrochemical cyclic voltammetry scans recorded for (a) $MoCeO_x$, (b) Co_{SA}-MoCeO and (c) Co_{SA}-$MoCeO_x$@BCT. Scan rates are 20, 40, 60, 80 and 100 mV s^{-1}. (d) Linear fitting of the capacitive currents versus cyclic voltammetry scans for these catalysts. (f) The calculated electrochemical active surface area values for $MoCeO_x$, Co_{SA}-$MoCeO_x$ and Co_{SA}-$MoCeO_x$@BCT.

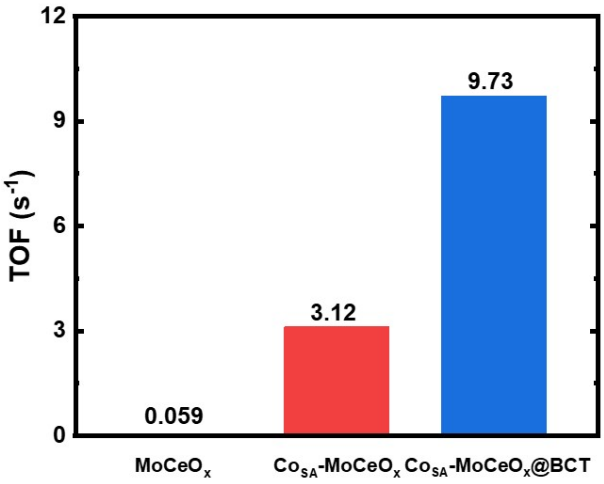

Fig. S30 The calculated turnover frequency values for Co sites on $MoCeO_x$, Co_{SA}-$MoCeO_x$ and Co_{SA}-$MoCeO_x$@BCT from the current density at overpotential of 250 mV.

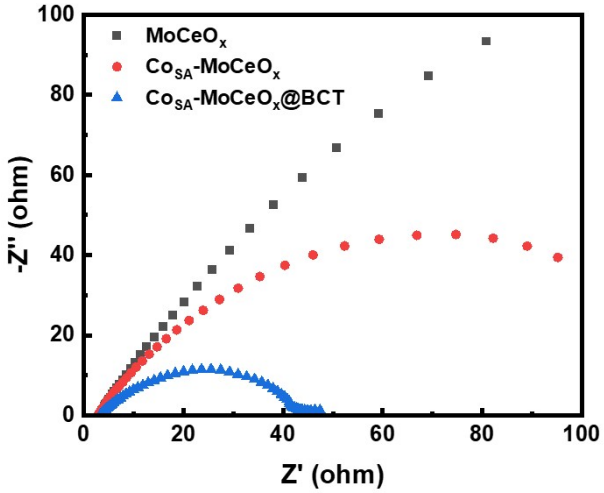

Fig. S31 Electrochemical impedance spectra at the 1.47 V vs. RHE for $MoCeO_x$, Co_{SA}-$MoCeO_x$ and Co_{SA}-$MoCeO_x$@BCT.

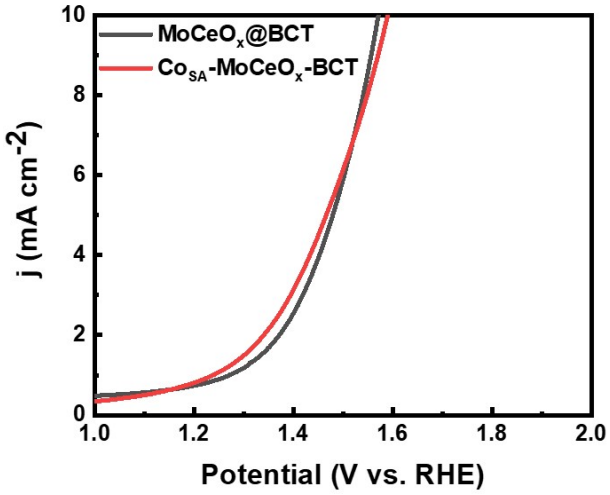

Fig. S32 OER activity of $MoCeO_x$@BCT and Co_{SA}-$MoCeO_x$-BCT in 0.5 M H_2SO_4.

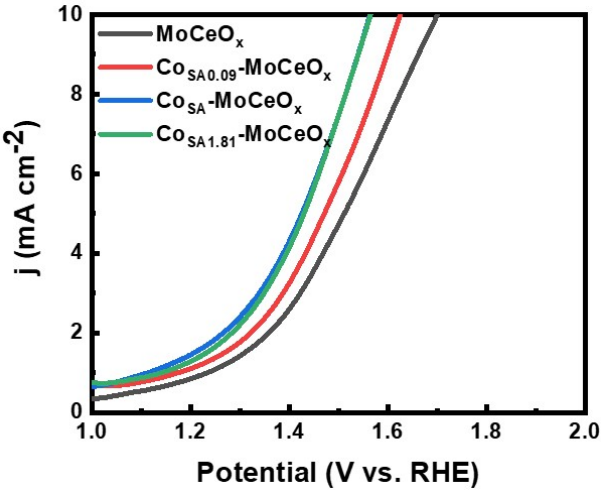

Fig. S33 OER activity of $MoCeO_x$, $Co_{SA0.09}$-$MoCeO_x$, Co_{SA}-$MoCeO_x$, and $Co_{SA1.81}$-$MoCeO_x$ in 0.5 M H_2SO_4.

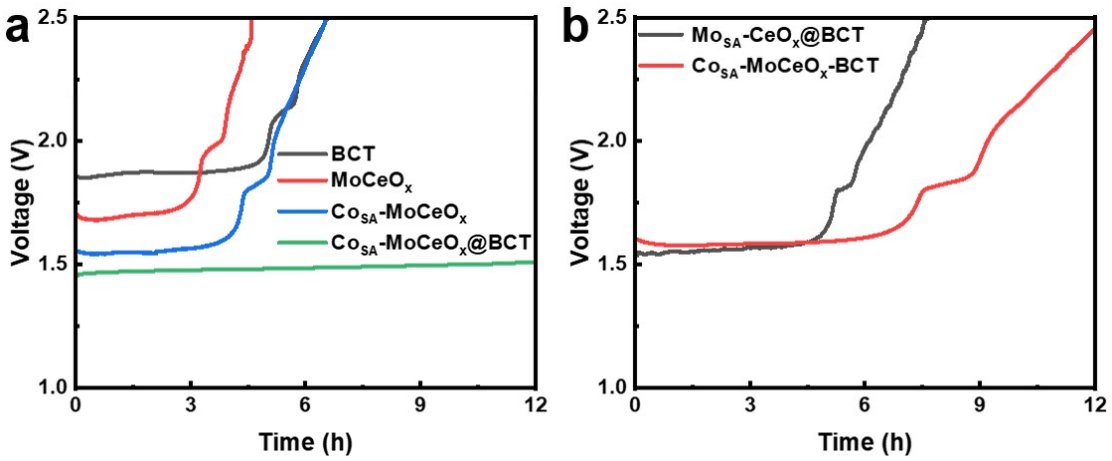

Fig. S34 Durability tests of BCT, $MoCeO_x$, Co_{SA}-$MoCeO_x$, Co_{SA}-$MoCeO_x$@BCT, Mo_{SA}-CeO_x@BCT and Co_{SA}-$MoCeO_x$-BCT (mechanically mixed) electrodes under a constant current density of 10 mA cm^{-2} for 12 h in 0.5 M H_2SO_4.

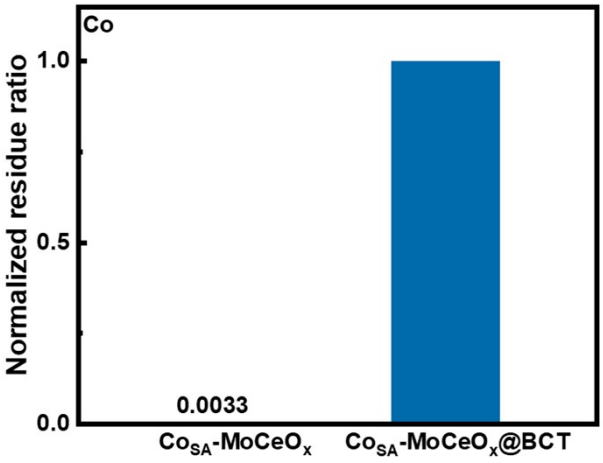

Fig. S35 Normalized residue of Co in Co_{SA}-$MoCeO_x$ and Co_{SA}-$MoCeO_x$@BCT after stability testing measured by ICP-OES.

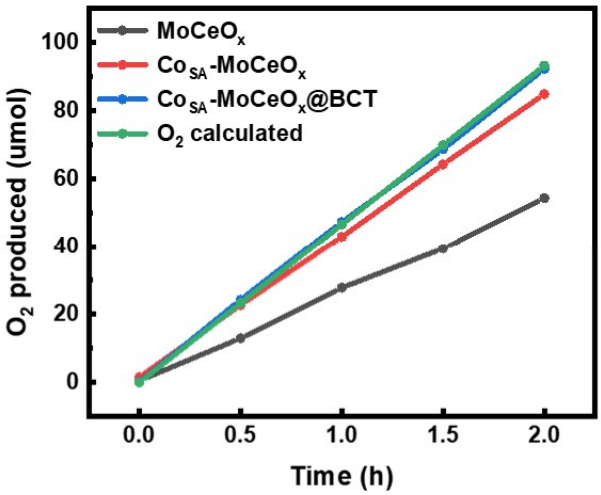

Fig. S36 The amount of oxygen theoretically calculated and experimentally measured versus time for $MoCeO_x$, Co_{SA}-$MoCeO_x$ and Co_{SA}-$MoCeO_x$@BCT at a current density of 10 mA cm^{-2}.

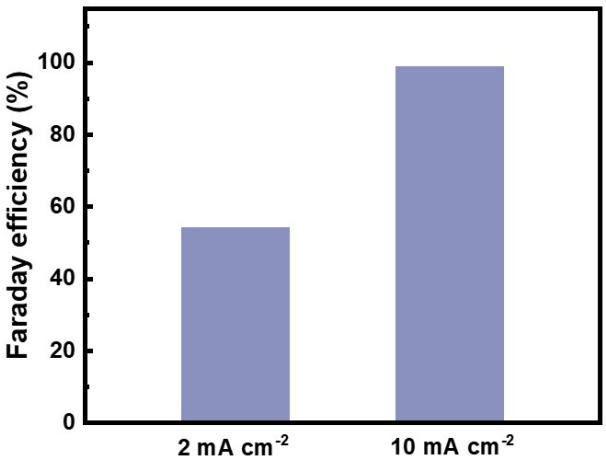

Fig. S37 O_2 Faraday efficiency for OER of Co_{SA}-$MoCeO_x$@BCT at a current density of 2 and 10 mA cm^{-2} in acidic solution of 0.5 M H_2SO_4, respectively.

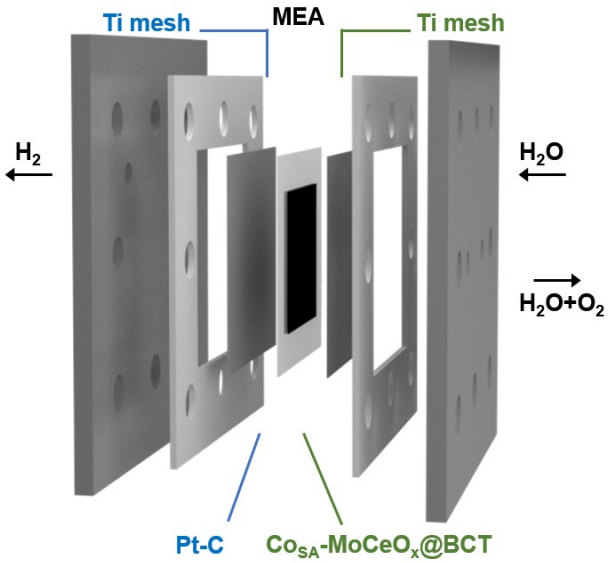

Fig. S38 Schematic diagram of the PEMWE.

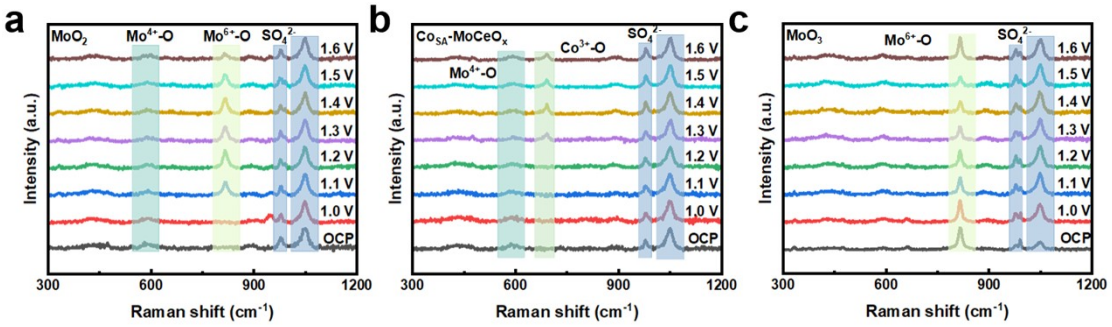

Fig. S39 *In situ* Raman spectra of (a) MoO_2, (b) Co_{SA}-$MoCeO_x$ and (c) MoO_3 under the applied potential range from 1.1 V to 1.6 V in acidic solution of 0.5 M H_2SO_4.

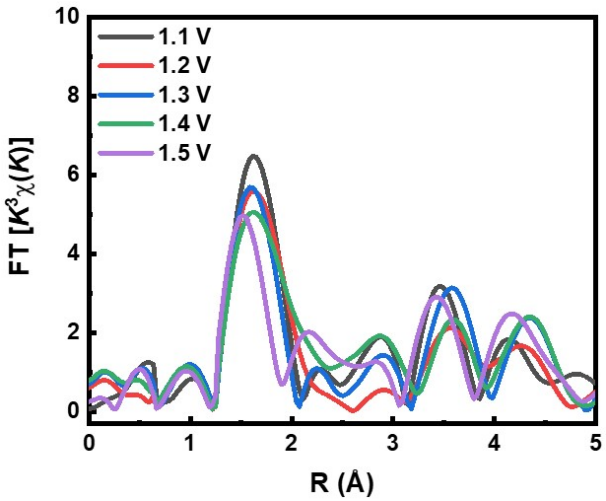

Fig. S40 Fourier transforms of k^3-weighted Co K-edge EXAFS spectra for r space of Co_{SA}-$MoCeO_x$ at applied voltages from 1.1 to 1.5 V.

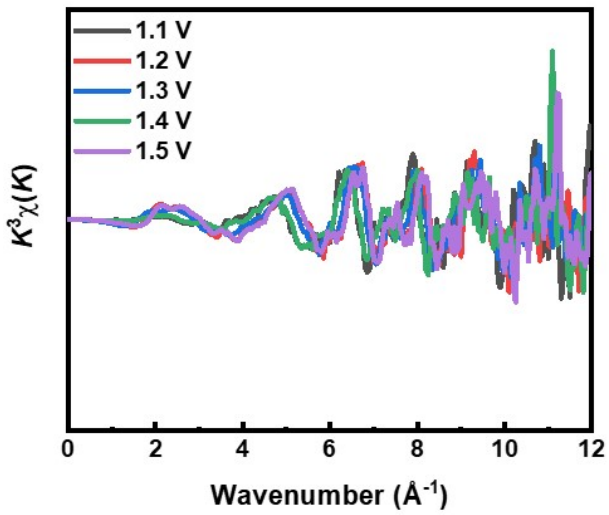

Fig. S41 Fourier transforms of k^3-weighted Co K-edge EXAFS spectra for k space of Co_{SA}-$MoCeO_x$ at applied voltages from 1.1 to 1.5 V.

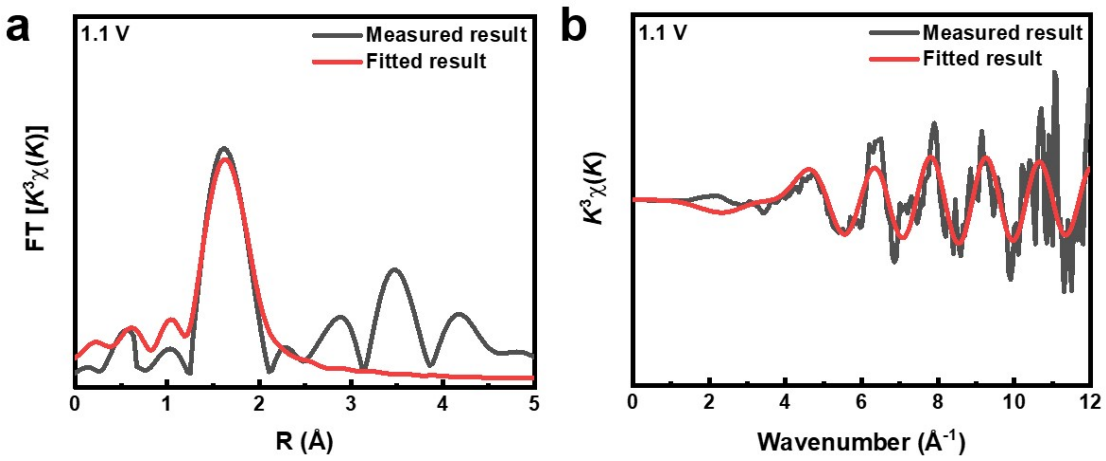

Fig. S42 k^3-weighted EXAFS. (a) r space, (b) k space fitting curves of Co_{SA}-$MoCeO_x$ at 1.1 V vs. RHE.

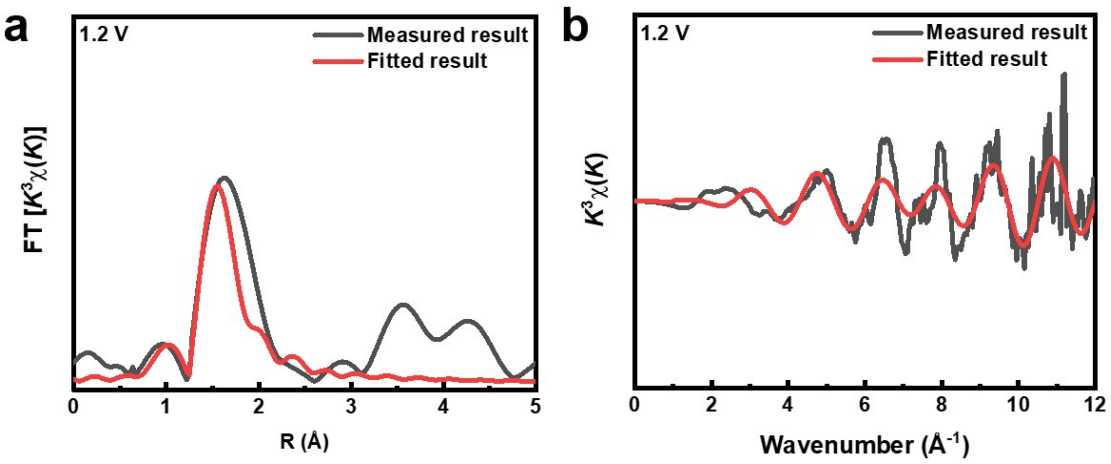

Fig. S43 k^3-weighted EXAFS. (a) r space, (b) k space fitting curves of Co_{SA}-$MoCeO_x$ at 1.2 V vs. RHE.

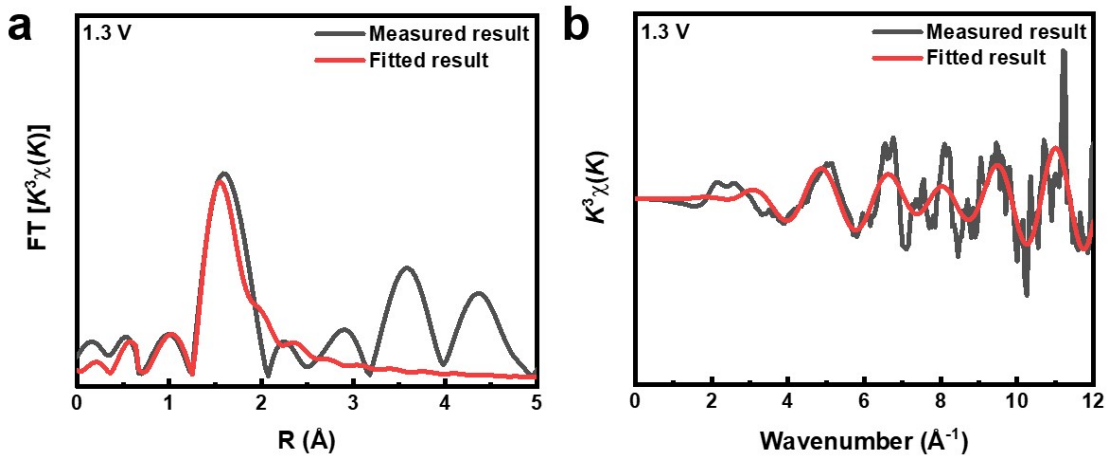

Fig. S44 k^3-weighted EXAFS. (a) r space, (b) k space fitting curves of Co_{SA}-$MoCeO_x$ at 1.3 V vs. RHE.

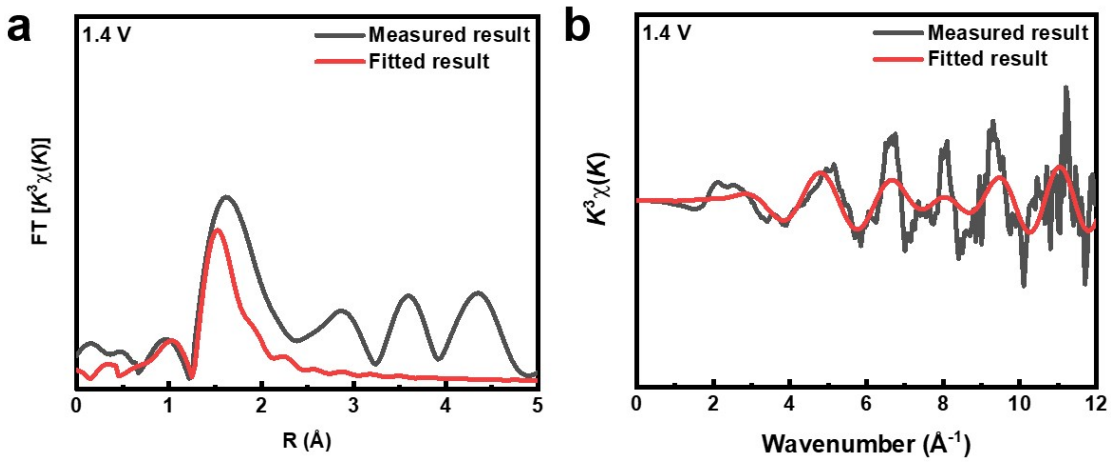

Fig. S45 k^3-weighted EXAFS. (a) r space, (b) k space fitting curves of Co_{SA}-$MoCeO_x$ at 1.4 V vs. RHE.

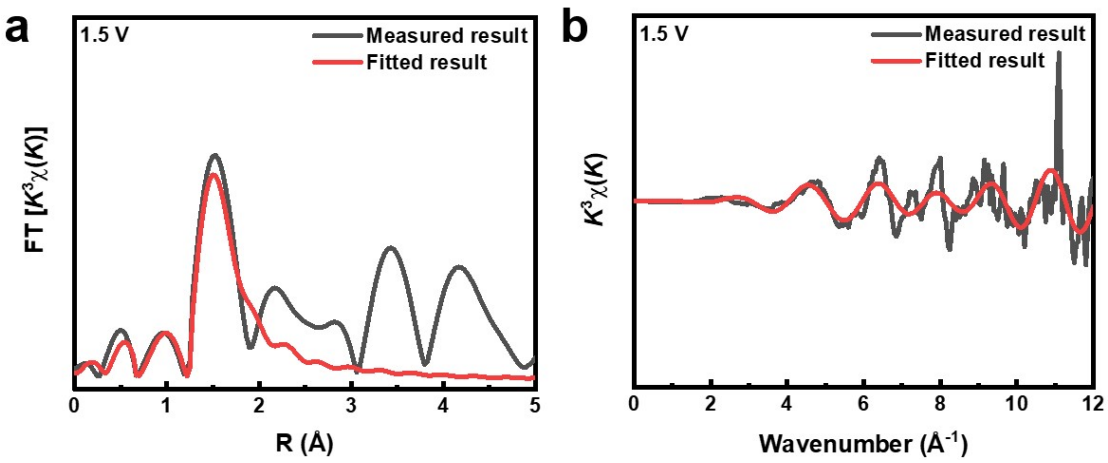

Fig. S46 k^3-weighted EXAFS. (a) r space, (b) k space fitting curves of Co_{SA}-$MoCeO_x$ at 1.5 V vs. RHE.

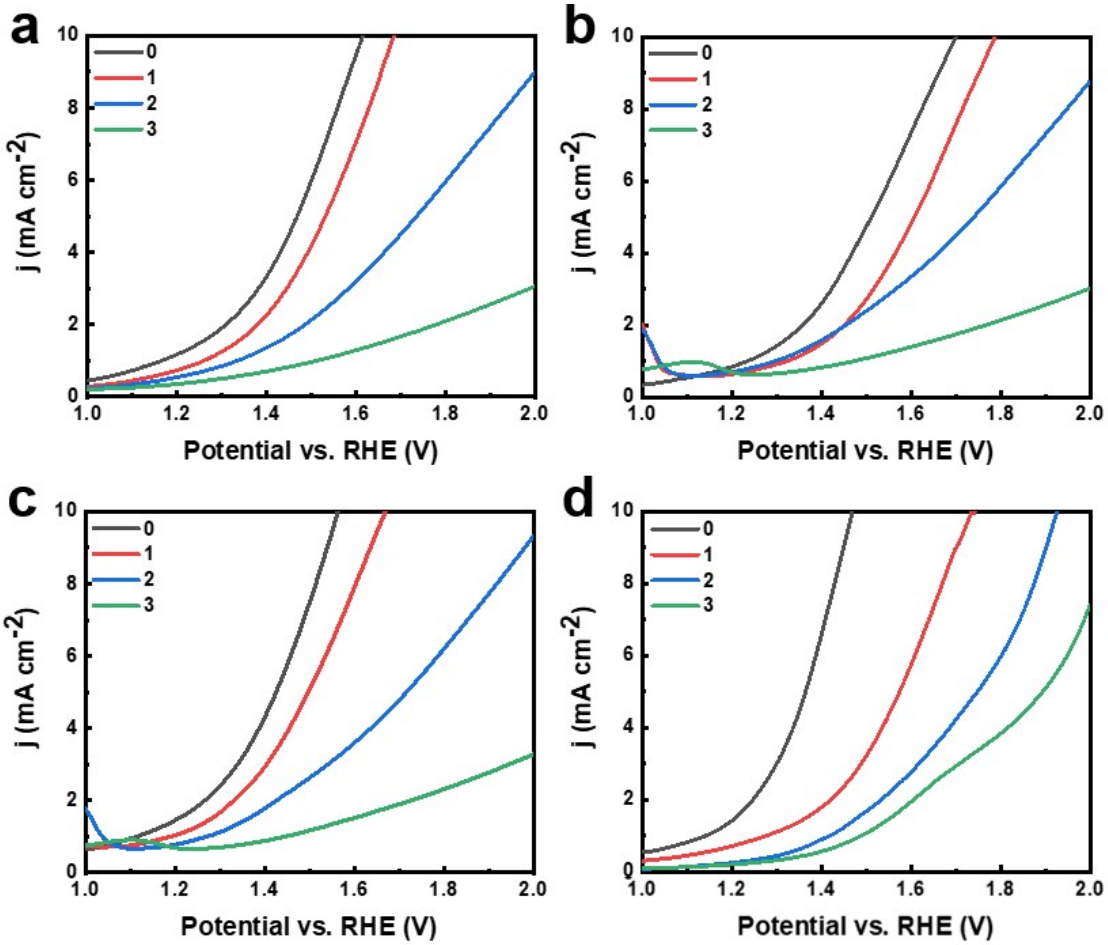

Fig. S47 OER activity of (a) MoO_3, (b) $MoCeO_x$, (c) Co_{SA}-$MoCeO_x$ and (d) Co_{SA}-$MoCeO_x$@BCT in acidic solutions with different pH.

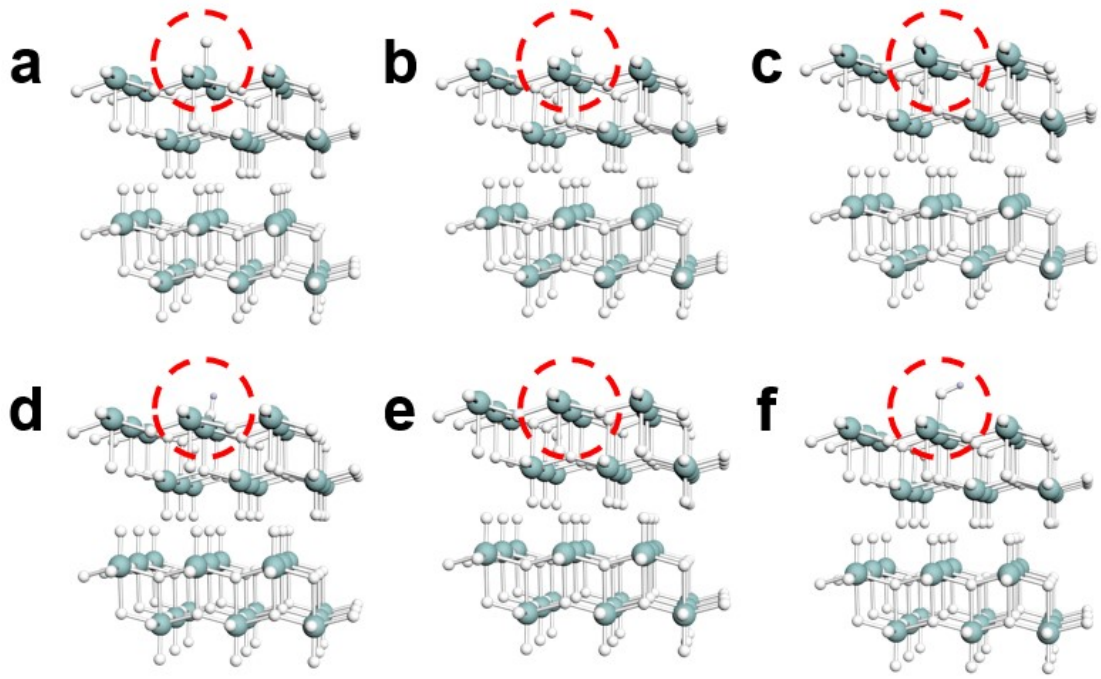

Fig. S48 The OER process follows LOM on MoO_3. (a) 2O*, (b) O_2*+V_O, (c) O_2+V_O, (d) OH*+V_O, (e) O*+V_O, and (f) O*+OH*, and the Mo, O, H are colored by green, white and purple, respectively. Red circles represent the intermediates on MoO_3 following the LOM.

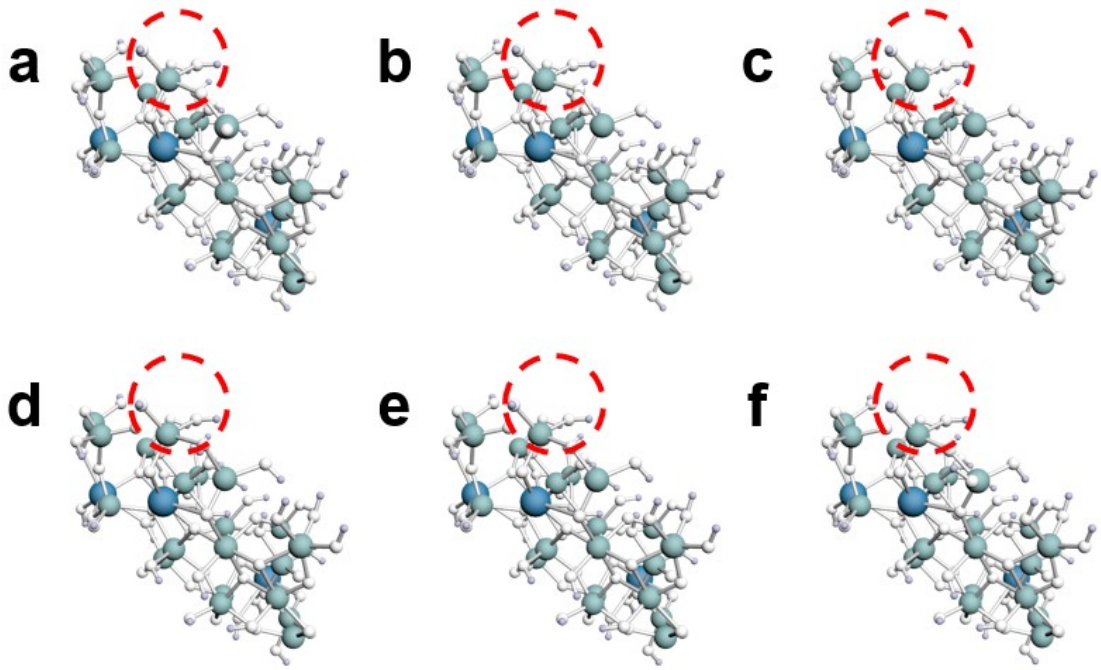

Fig. S49 The OER process follows LOM on $MoCeO_x$. (a) 2O*, (b) O_2*+V_O, (c) O_2+V_O, (d) OH*+V_O, (e) O*+V_O, and (f) O*+OH*, and the Mo, Ce, O, H are colored by green, blue, white and purple, respectively. Red circles represent the intermediates on $MoCeO_x$ following the LOM.

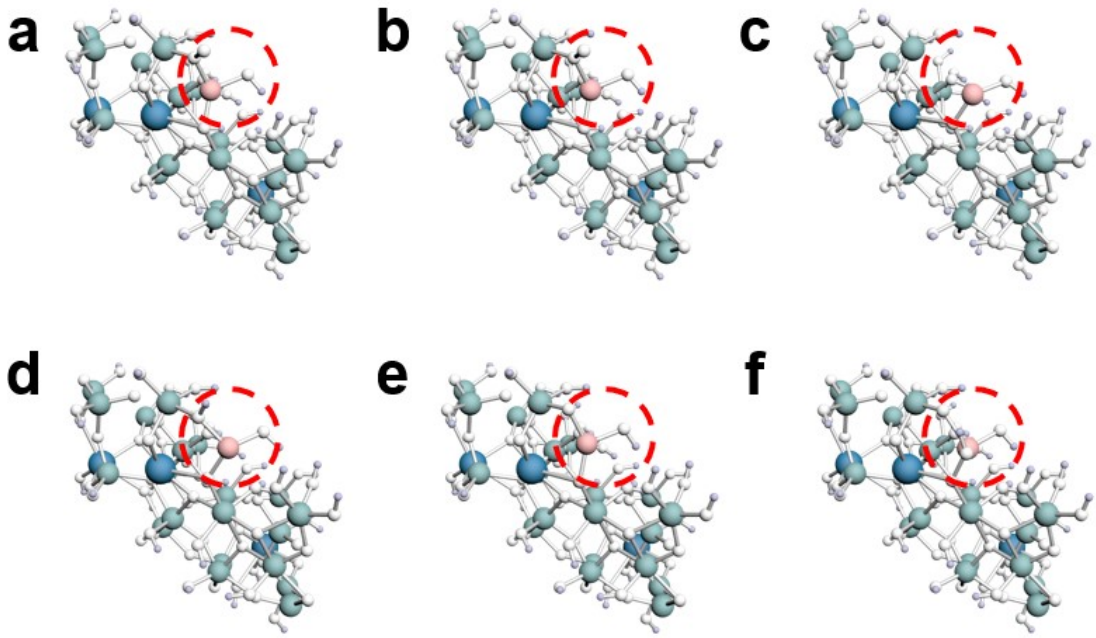

Fig. S50 The OER process follows LOM on $CoMoCeO_x$. (a) 2O*, (b) O_2*+V_O, (c) O_2+V_O, (d) OH*+V_O, (e) O*+V_O, and (f) O*+OH*, and the Mo, Ce, Co, O, H are colored by green, blue, red, white and purple, respectively. Red circles represent the intermediates on Co_{SA}-$MoCeO_x$ following the LOM.

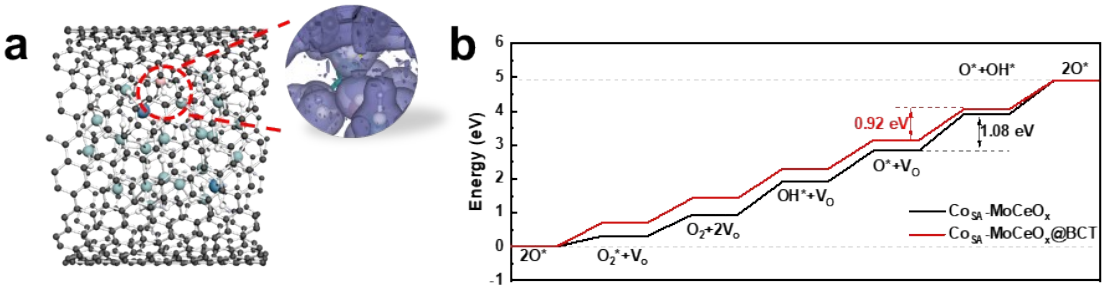

Fig. S51 (a) Calculation models and the electronic distributions of Co_{SA}-$MoCeO_x$@BCT. (b) OER calculation results of Co_{SA}-$MoCeO_x$ and Co_{SA}-$MoCeO_x$@BCT.

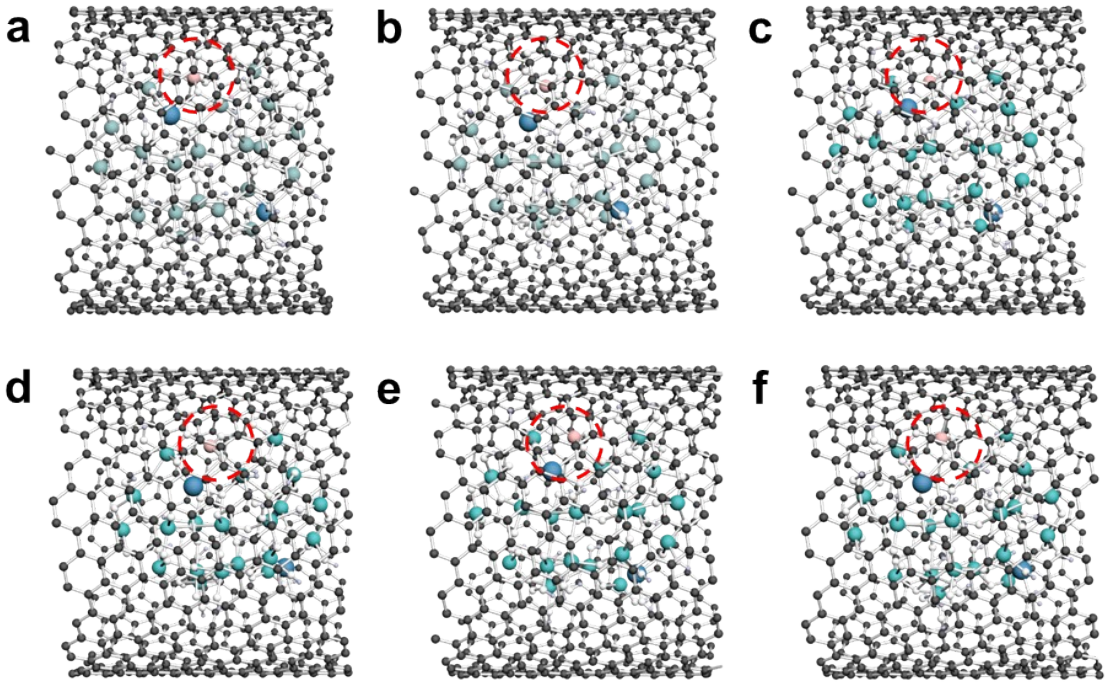

Fig. S52 The OER process follows LOM on Co_{SA}-$MoCeO_x$@BCT. (a) 2O*, (b) O_2*+V_O, (c) O_2+V_O, (d) OH*+V_O, (e) O*+V_O, and (f) O*+OH*, and the Mo, O, H are colored by green, white and purple, respectively. Red circles represent the intermediates on Co_{SA}-$MoCeO_x$@BCT following the LOM.

Table S1. Co content in metallic elements of amorphous Mo-Ce oxides supported single-atom Co catalysts coated with bamboo-like carbon nanotubes according to XRF characterization.

Sample	Chemical composition	Co (At %)	Mo (At %)	Ce (At %)
1	$MoCeO_x$	0	86.04	13.96
2	$Co_{SA0.09}$-$MoCeO_x$	0.09	88.49	11.42
3	Co_{SA}-$MoCeO_x$	1.77	88.34	9.89
4	$Co_{SA1.81}$-$MoCeO_x$	1.81	82.90	15.29
5	Co_{SA}-$MoCeO_x$@BCT	1.71	86.59	11.70

Table S2. EXAFS fitting parameters at the Mo K-edge for various samples.

Sample	Path	C.N.	R (Å)	σ^2 (Å^2)	R-factor
MoO_2	Mo-O	6	1.60	0.0128	0.00071
	Mo-Mo	6	2.20	0.0056	
$MoCeO_x$	Mo-O	5.22	1.16	0.0136	0.00078
Co_{SA}-$MoCeO_x$	Mo-O	5.15	1.15	0.0094	0.00061
MoO_3	Mo-O	6	1.13	0.0030	0.00053
	Mo-Mo	6	1.70	0.0055	

Table S3. EXAFS fitting parameters at the Co K-edge for various samples.

Sample	Path	C.N.	R (Å)	σ^2 (Å^2)	R-factor
CoO	Co-O	4	1.71	0.0138	0.00088
	Co-Co	12	2.70	0.0053	
Co_{SA}-$MoCeO_x$	Co-O	5.08	1.69	0.0135	0.00114
Co_2O_3	Co-O	6	1.50	0.0093	0.00086
	Co-Co	12	2.51	0.0081	

Table S4. EXAFS fitting parameters at the Mo K-edge for Co_{SA}-$MoCeO_x$@BCT.

Sample	Path	C.N.	R (Å)	σ^2 (Å^2)	R-factor
Co_{SA}-$MoCeO_x$@BCT	Mo-O	5.09	1.16	0.0136	0.00089

Table S5. EXAFS fitting parameters at the Co K-edge for Co_{SA}-$MoCeO_x$@BCT.

Sample	Path	C.N.	R (Å)	σ^2 (Å^2)	R-factor
Co_{SA}-$MoCeO_x$@BCT	Co-N	3.89	1.40	0.099	0.000106
	Co-O	5.09	1.67	0.078	

Table S6. Comparison of OER performance for Co_{SA}-$MoCeO_x$@BCT and recently reported catalysts in acidic solution of 0.5 M H_2SO_4.

Catalysts	Electrolyte	j (mA/cm^2)	ŋ required (mV)	Stability (at 10 mA cm^{-2})	Ref
Co_{SA}-$MoCeO_x$@BCT	0.5 M H_2SO_4	10	239	60 h	This work
La/Mn co-doped cobalt spinel (LMCF)	0.1 M $HClO_4$	10	353	360 h	[6]
Co_2MnO_4	0.5 M H_2SO_4	10	395	320 h at 100 mA cm^{-2}_{geo}	[7]
$CoFePbO_x$	0.05 M H_2SO_4	10	700	10 h	[8]
Ba[Co-POM]	1 M H_2SO_4	10	500	24 h at 250 mV	[9]
CeO_2/Co_3O_4	0.5 M H_2SO_4	10	347	50 h	[10]
$Mn_{7.5}O_{10}Br_3$	0.5 M H_2SO_4	10	295	300 h at 100 mA cm^{-2}	[11]
$Co_{3-x}Ba_xO_4$	0.5 M H_2SO_4	10	278	110 h	[12]
$Ni_{0.5}Mn_{0.5}Sb_{1.7}O_y$	1 M H_2SO_4	10	672	168 h	[13]
γ-MnO_2/FTO	1 M H_2SO_4	10	428	8000 h at 100 mA cm^{-2}	[14]
Mo-Co_9S_8@C	0.5 M H_2SO_4	10	370	24 h	[15]
NiCo-nitrides/$NiCo_2O_4$/	0.5 M H_2SO_4	10	432	---	[16]

GF					
$CeO_2/Co_2NiP_{0.03}O_x$	0.5 M H_2SO_4	10	262	50 h at 5 mA cm^{-2}	[17]
$Mn_{0.67}Sb_{0.33}O_2$	1 M H_2SO_4	10	520	~30 h	[18]
C coated Co_3O_4	0.5 M H_2SO_4	10	370	86.8 h at 100 mA cm^{-2}	[19]
Ag doped Co_3O_4	0.5 M H_2SO_4	10	470	10 h	[20]
Co_3O_4/FTO	0.5 M H_2SO_4	10	570	10 h	[21]

Table S7. EXAFS fitting parameters at the Co K-edge for Co_{SA}-$MoCeO_x$ at applied voltages from 1.1 to 1.5 V.

Sample	Path	C.N.	R (Å)	σ^2 (Å^2)	R-factor
Co_{SA}-$MoCeO_x$ (1.1 V)	Co-O	5.02	1.64	0.0112	0.00113
Co_{SA}-$MoCeO_x$ (1.2 V)	Co-O	4.94	1.61	0.0141	0.00129
Co_{SA}-$MoCeO_x$ (1.3 V)	Co-O	4.91	1.58	0.0126	0.00120
Co_{SA}-$MoCeO_x$ (1.4 V)	Co-O	4.88	1.54	0.0170	0.00145
Co_{SA}-$MoCeO_x$ (1.5 V)	Co-O	4.80	1.52	0.0109	0.0097

References

1. Garrido Ribó, E., Bell, N.L., Xuan, W., Luo, J., Long, D.-L., Liu, T., and Cronin, L. (2020). Synthesis, Assembly, and Sizing of Neutral, Lanthanide Substituted Molybdenum Blue Wheels {Mo90Ln10}. J. Am. Chem. Soc. 142, 17508-17514. 10.1021/jacs.0c07146.
2. Kresse, G., and Furthmüller, J. (1996). Efficiency of ab-initio total energy calculations for metals and semiconductors using a plane-wave basis set. Comput. Mater. Sci. 6, 15-50. 10.1016/0927-0256(96)00008-0.
3. Kresse, G., and Furthmüller, J. (1996). Efficient iterative schemes for ab initio total-energy calculations using a plane-wave basis set. Phys. Rev. B 54, 11169-11186. 10.1103/PhysRevB.54.11169.
4. Perdew, J.P., Burke, K., and Ernzerhof, M. (1996). Generalized Gradient Approximation Made Simple. Phys. Rev. Lett. 77, 3865-3868. 10.1103/PhysRevLett.77.3865.
5. Blöchl, P.E. (1994). Projector augmented-wave method. Phys. Rev. B 50, 17953-17979. 10.1103/PhysRevB.50.17953.
6. Chong, L., Gao, G., Wen, J., Li, H., Xu, H., Green, Z., Sugar, J.D., Kropf, A.J., Xu, W., Lin, X.-M., et al. (2023). La- and Mn-doped cobalt spinel oxygen evolution catalyst for proton exchange membrane electrolysis. Science 380, 609-616. 10.1126/science.ade1499.
7. Li, A., Kong, S., Guo, C., Ooka, H., Adachi, K., Hashizume, D., Jiang, Q., Han, H., Xiao, J., and Nakamura, R. (2022). Enhancing the stability of cobalt spinel oxide towards sustainable oxygen evolution in acid. Nat. Catal. 5, 109-118. 10.1038/s41929-021-00732-9.
8. Chatti, M., Gardiner, J.L., Fournier, M., Johannessen, B., Williams, T., Gengenbach, T.R., Pai, N., Nguyen, C., MacFarlane, D.R., Hocking, R.K., and Simonov, A.N. (2019). Intrinsically stable in situ generated electrocatalyst for long-term oxidation of acidic water at up to 80 °C. Nat. Catal. 2, 457-465. 10.1038/s41929-019-0277-8.
9. Blasco-Ahicart, M., Soriano-López, J., Carbó, J.J., Poblet, J.M., and Galan-Mascaros, J.R. (2018). Polyoxometalate electrocatalysts based on earth-abundant metals for efficient water oxidation in acidic media. Nat. Chem. 10, 24-30. 10.1038/nchem.2874.
10. Huang, J., Sheng, H., Ross, R.D., Han, J., Wang, X., Song, B., and Jin, S. (2021). Modifying redox properties and local bonding of Co_3O_4 by CeO_2 enhances oxygen evolution catalysis in acid. Nat. Commun. 12, 3036. 10.1038/s41467-021-23390-8.
11. Pan, S., Li, H., Liu, D., Huang, R., Pan, X., Ren, D., Li, J., Shakouri, M., Zhang, Q., Wang, M., et al. (2022). Efficient and stable noble-metal-free catalyst for acidic water oxidation. Nat. Commun. 13, 2294. 10.1038/s41467-022-30064-6.
12. Wang, N., Ou, P., Miao, R.K., Chang, Y., Wang, Z., Hung, S.-F., Abed, J., Ozden, A., Chen, H.-Y., Wu, H.-L., et al. (2023). Doping Shortens the Metal/Metal Distance and Promotes OH Coverage in Non-Noble Acidic Oxygen Evolution Reaction Catalysts. J. Am. Chem. Soc. 145, 7829-7836. 10.1021/jacs.2c12431.
13. Moreno-Hernandez, I.A., MacFarland, C.A., Read, C.G., Papadantonakis, K.M., Brunschwig, B.S., and Lewis, N.S. (2017). Crystalline nickel manganese antimonate as a stable water-oxidation catalyst in aqueous 1.0 M H2SO4. Energy Environ. Sci. 10, 2103-2108. 10.1039/C7EE01486D.
14. Li, A., Ooka, H., Bonnet, N., Hayashi, T., Sun, Y., Jiang, Q., Li, C., Han, H., and Nakamura,

R. (2019). Stable Potential Windows for Long-Term Electrocatalysis by Manganese Oxides Under Acidic Conditions. Angew. Chem. Int. Ed. 58, 5054-5058. 10.1002/anie.201813361.

15. Wang, L., Duan, X., Liu, X., Gu, J., Si, R., Qiu, Y., Qiu, Y., Shi, D., Chen, F., Sun, X., et al. (2020). Atomically Dispersed Mo Supported on Metallic Co_9S_8 Nanoflakes as an Advanced Noble-Metal-Free Bifunctional Water Splitting Catalyst Working in Universal pH Conditions. Adv. Energy Mater. 10, 1903137. 10.1002/aenm.201903137.
16. Liu, Z., Tan, H., Liu, D., Liu, X., Xin, J., Xie, J., Zhao, M., Song, L., Dai, L., and Liu, H. (2019). Promotion of Overall Water Splitting Activity Over a Wide pH Range by Interfacial Electrical Effects of Metallic NiCo-nitrides Nanoparticle/$NiCo_2O_4$ Nanoflake/graphite Fibers. Adv. Sci. 6, 1801829. 10.1002/advs.201801829.
17. Liu, J., Wang, T., Liu, X., Shi, H., Li, S., Xie, L., Cai, Z., Han, J., Huang, Y., Wang, G., and Li, Q. (2023). Reducible Co3+–O Sites of Co–Ni–P–Ox on CeO2 Nanorods Boost Acidic Water Oxidation via Interfacial Charge Transfer-Promoted Surface Reconstruction. ACS Catal. 13, 5194-5204. 10.1021/acscatal.2c06133.
18. Zhou, L., Shinde, A., Montoya, J.H., Singh, A., Gul, S., Yano, J., Ye, Y., Crumlin, E.J., Richter, M.H., Cooper, J.K., et al. (2018). Rutile Alloys in the Mn–Sb–O System Stabilize Mn3+ To Enable Oxygen Evolution in Strong Acid. ACS Catal. 8, 10938-10948. 10.1021/acscatal.8b02689.
19. Yang, X., Li, H., Lu, A.-Y., Min, S., Idriss, Z., Hedhili, M.N., Huang, K.-W., Idriss, H., and Li, L.-J. (2016). Highly acid-durable carbon coated Co_3O_4 nanoarrays as efficient oxygen evolution electrocatalysts. Nano Energy 25, 42-50. 10.1016/j.nanoen.2016.04.035.
20. Yan, K.-L., Qin, J.-F., Lin, J.-H., Dong, B., Chi, J.-Q., Liu, Z.-Z., Dai, F.-N., Chai, Y.-M., and Liu, C.-G. (2018). Probing the active sites of Co3O4 for the acidic oxygen evolution reaction by modulating the Co2+/Co3+ ratio. J. Mater. Chem. A 6, 5678-5686. 10.1039/C8TA00070K.
21. Mondschein, J.S., Callejas, J.F., Read, C.G., Chen, J.Y.C., Holder, C.F., Badding, C.K., and Schaak, R.E. (2017). Crystalline cobalt oxide films for sustained electrocatalytic oxygen evolution under strongly acidic conditions. Chem. Mater. 29, 950-957. 10.1021/acs.chemmater.6b02879.